

(2)

AFOSR-TR. 86-0555

AD-A170 837

DIRECT WRITING OF MICROSTRUCTURES  
FOR SOLID-STATE ELECTRONICS

Columbia Microelectronics Sciences Laboratories

Columbia University

Final Report

for

Approved for public release,  
distribution unlimited

Defense Advanced Projects Agency

and

Air Force Office of Scientific Research

1 February 1984 - 31 January 1986

R. M. Osgood, Jr.

Principal Investigator

DTIC  
ELECTE  
AUG 12 1986  
S D  
B

DTIC FILE COPY

86 8 8 062

UNCLASSIFIED

SECURITY CLASSIFICATION OF THIS PAGE

AD A170 837

(2)

## REPORT DOCUMENTATION PAGE

1a. REPORT SECURITY CLASSIFICATION <b>UNCLASSIFIED</b>		1b. RESTRICTIVE MARKINGS	
2a. SECURITY CLASSIFICATION AUTHORITY		3. DISTRIBUTION/AVAILABILITY OF REPORT Approved for public release; distribution unlimited	
2b. DECLASSIFICATION/DOWNGRADING SCHEDULE			
4. PERFORMING ORGANIZATION REPORT NUMBER(S) Final Report #2		5. MONITORING ORGANIZATION REPORT NUMBER(S) <b>AFOSR-TR- 86-0555</b>	
6a. NAME OF PERFORMING ORGANIZATION Columbia University/ Osgood Dept. of Electrical Engineering	6b. OFFICE SYMBOL (If applicable)	7a. NAME OF MONITORING ORGANIZATION Office of Projects and Grants Columbia University	
6c. ADDRESS (City, State and ZIP Code) 1330 Mudd Building - Columbia University 520 West 120th Street New York, New York 10027		7b. ADDRESS (City, State and ZIP Code) Box 20 Low Memorial Library/ Columbia University New York, New York 10027	
8a. NAME OF FUNDING/SPONSORING ORGANIZATION <b>AFOSR</b>	8b. OFFICE SYMBOL (If applicable) <b>NP</b>	9. PROCUREMENT INSTRUMENT IDENTIFICATION NUMBER F49620-84-C-0022	
8c. ADDRESS (City, State and ZIP Code) Air Force Office of Scientific Research Building 401/Bolling AFB DC 20332		10. SOURCE OF FUNDING NOS.	
		PROGRAM ELEMENT NO.	PROJECT NO.
		TASK NO.	WORK UNIT NO.
11. TITLE (Include Security Classification) Direct Writing of Microstructures for <b>SOLID-STATE</b> <b>ELECTRONICS</b>		11100F	2301
12. PERSONAL AUTHOR(S) Richard M. Osgood, Jr.		A1	N/A
13a. TYPE OF REPORT FINAL	13b. TIME COVERED FROM 840201 TO 860131	14. DATE OF REPORT (Yr., Mo., Day) 860419	15. PAGE COUNT 49
16. SUPPLEMENTARY NOTATION			
17. COSATI CODES		18. SUBJECT TERMS (Continue on reverse if necessary and identify by block number)	
FIELD	GROUP	SUB. GR.	
		Direct Writing/Microstructures/ MICROELECTRONICS	
19. ABSTRACT (Continue on reverse if necessary and identify by block number)			
<p>This report summarizes two years of research on new laser processing techniques on opto- and microelectronics. The main results are in 1) the demonstration of UV laser direct writing of low resistivity metal lines, and the subsequent demonstration of the usefulness of laser writing (via deposition) in the reconfiguring of an LSI circuitry; and 2) the discovery, characterization, and understanding of the techniques of light-guided etching for the fabrication of ultra-high-aspect-ratio microelectronics structures. In the case of light-guided etching, an application of the technique to optical interconnects has already been demonstrated.</p>			
20. DISTRIBUTION/AVAILABILITY OF ABSTRACT UNCLASSIFIED/UNLIMITED <input checked="" type="checkbox"/> SAME AS RPT. <input checked="" type="checkbox"/> DTIC USERS <input type="checkbox"/>		21. ABSTRACT SECURITY CLASSIFICATION <b>UNCLASSIFIED</b>	
22a. NAME OF RESPONSIBLE INDIVIDUAL <b>HOWARD R. SCHLOSSBERG</b>		22b. TELEPHONE NUMBER (Include Area Code) 802/762-4906	22c. OFFICE SYMBOL

DL RM 1473, 83 APR

EDITION OF 1 JAN 73 IS OBSOLETE.

UNCLASSIFIED  
SECURITY CLASSIFICATION OF THIS PAGE



Sponsored by

Advance Research Projects Agency

- (1) ARPA Order 4487
- (2) Program Code FQ8671
- (3) The Trustees of Columbia University in the City of New York
- (4) Start Date: February 01, 1984 **AIR FORCE OFFICE OF SCIENTIFIC RESEARCH (AFSC)**
- (5) End Date: ~~December~~ **JANUARY** 31, 1986 **NOTICE OF TRANSMITTAL TO DTIC**  
This technical report has been reviewed and is approved for public release IAW AFR 190-12. Distribution is unlimited.  
**MATTHEW J. KERPER**  
Chief, Technical Information Division
- (6) Contract Amount: \$525,198.00
- (7) Contract Number: F49620-84-C-0022
- (8) Principal Investigator: Richard M. Osgood, Jr.  
Telephone: (212) 280-4462
- (9) Program Manager: Dr. Howard Schlossberg  
Dr. John Neff  
Telephone: (202) 767-4906
- (10) Title: DIRECT WRITING OF MICROSTRUCTURES FOR ~~MICROELECTRONICS~~ **SOLID-STATE ELECTRONICS**

The views and conclusions contained in this document are those of the authors and should not be interpreted as necessarily representing the official policies, either expressed or implied, of the Defense Advanced Research Projects Agency or the U.S. Government.



TITLE ON  
COVER CORRECT

<input checked="checked" type="checkbox"/>	
<input type="checkbox"/>	
<input type="checkbox"/>	
PER CALL JC	
By _____	
Distribution/	
Availability Codes	
Dist	Avail and/or Special
A-1	

## TABLE OF CONTENTS

I. <u>INTRODUCTION</u> .....	1.
II. <u>DIRECT WRITING OF METAL CONDUCTORS</u> .....	1.
A. Upgrading of the Deposition Apparatus.....	1.
B. Electrical Properties of Photodeposited Lines.....	2.
1. Introduction.....	2.
2. Indium Deposition.....	2.
3. Aluminum Deposition.....	3.
4. Contact Formation on Aluminum.....	5.
C. Application of Photodeposition.....	6.
D. Deposition of Refractory Metals.....	7.
1. Deposition of Tungsten.....	7.
2. Deposition of Molybdenum from $\text{Mo(CO)}_6$ .....	9.
E. Detailed Investigation of Processes Occurring in Deposition of $\text{DeZn}$ , to Provide a Specific Theory of Photodeposition.....	10.
III. <u>DIRECT FABRICATION OF DIFFRACTION GRATINGS</u> .....	17.
A. Growth of Submicrometer Gratings.....	17.
1. Resonant Growth of Metal Gratings.....	17.
2. Fabrication of Deep, Ultrahigh-Aspect-Ratio, Diffraction Gratings.....	19.
B. Direct Fabrication of Optical Structures.....	20.
1. Light-Guided Microfabrication.....	20.
2. Aqueous Etching of Semiconductors Using Pulsed Ultraviolet Lasers.....	25.
3. Theory of Light Guided Etching.....	25.
4. Silicon Etching.....	26.
5. Waveguided Etching of $\text{InP}$ .....	27.
IV. <u>FIGURE CAPTIONS</u> .....	30.
V. <u>PAPERS SUBMITTED FOR PUBLICATION</u> .....	31.
VI. <u>PRESENTATIONS TO INDUSTRY AND PROFESSIONAL ORGANIZATIONS</u> .....	32.

## I. INTRODUCTION

This report summarizes two years of research on new laser processing techniques for opto- and microelectronics. The main results are in 1) the demonstration of UV laser direct writing of low resistivity metal lines, and the subsequent demonstration of the usefulness of UV laser writing (via photodeposition) in the reconfiguring of an LSI circuitry; and 2) the discovery, characterization, and understanding of the technique of light-guided etching for the fabrication of ultrahigh-aspect-ratio microelectronics structures. In the case of light-guided etching, an application of the technique to optical interconnects has already been demonstrated.

During the period of the contract, two graduate students, Robert Krchnavek and Dragan Podlesnik completed their Ph.D. Thesis work. Both have been supported by this DARPA/AFOSR contract, Krchnavek in laser direct writing, and Podelsnik in light guided etching, respectively. In addition, the contract research has resulted in publications and talks at industrial and professional symposia and conferences.

Work in the two major areas described here has engendered considerable interest in the industrial community. For example, our results in direct writing of metal conductors were of great interest to IBM for application to reconfiguring and repairing of ceramic package metallization. This interest was made tangible by their supplying matching funds for direct writing of tungsten.

## II. DIRECT WRITING OF METAL CONDUCTORS

### A. Upgrading of the Deposition Apparatus.

In preparation for our experimental work on the deposition of refractory metals, we began a series of changes in our laser-writing apparatus. The first change was to replace the broadband, Zeiss-microscope, beam splitter with an

optimized dielectric splitter mounted near the microscope objective. Second, a gas-flow system was developed for the translating gas-sample cell. Finally, we have developed several sample cell designs for operating at elevated substrate temperatures. This upgraded apparatus was then tested using trimethylaluminum and triisobutylaluminum carrier gases. Deposition from these gases was observed; however, a low background pressure of  $O_2$  resulted in oxidation of the aluminum in situ. To reduce this problem we installed a cryopump so as to reduce the  $O_2$  background pressure.

## B. Electrical Properties of Photodeposited Lines

### 1. Introduction

For most applications of laser direct writing, the electrical and optical properties of the deposited material must be well characterized and adequate for the application at hand. Unfortunately this aspect of laser-induced material growth has heretofore received very little attention - chiefly because the main concern has thus far been the spatial resolution and basic material of the deposit. In this research program, we are devoting a major portion of the resources to achieving reproducibly good photodeposited material, and then, to showing the application of various photodeposition systems to device applications.

### 2. Indium Deposition

Our initial efforts on measurements of the electrical resistance were concerned with interconnects of indium photodeposited from trimethylindium (TMIn). Indium is a soft metal with a low melting point, useful as a soldering material in IC-packaging.

Photodeposition from a trivalent-metal compound has the added advantage of giving insight into the photodeposition physics of aluminum-type metallorganic

compounds. Despite its importance, deposition of aluminum has been very difficult to study directly because of its propensity for reaction with adsorbed  $H_2O$ ,  $OH$  or residual oxygen (see below).

The experiments were done with lines which had a typical width of  $3\mu m$  and connected to two gold islands separated by  $100\mu m$ . The line resistivity was found by optically measuring their length and width and by determining their thickness with a mechanical profilometer. The resistivity of the line was normalized with the corresponding resistivity of the bulk material. This technique was difficult to develop because of the step coverage problems at the edge of the gold pads. Several groups in industry have subsequently adopted it for their laser writing experiments.

The results for the indium deposition at different trimethylindium (TMIn) gas pressures and two power levels are shown in Fig. 1. For both curves a distinct minimum occurs at 1.25 Torr. In the low pressure regime, scanning electron micrographs reveal that grains are formed by surface electromagnetic waves. We believe that this effect give rise to the increased resistivity. At high pressures (above 1.25 Torr, which is one half of the TMIn vapor pressure at room temperature), the deposition occurs primarily from a liquid-like adlayer, which increases the impurity content and, therefore, the metal resistivity. At low power densities the grain formation and incomplete decomposition of the adlayer are increased, both of which lead to increased film resistivity.

### 3. Aluminum Deposition

Aluminum is a basic "building block" material for current microelectronics technology, since the final level of metallization on IC's is an evaporated aluminum film. As a result, direct writing of aluminum needs to be developed for IC repair work; in some cases use of other directly written materials on Al would cause intermetallic diffusion and unstable interconnections. We began our investigation

with trimethylaluminum (TMAI) in a static filled cell. The doubled  $\text{Ar}^+$  laser light at 257 nm was used in our experiments. Recently made absorption spectra of the compound reveals that at this wavelength, the gas is highly transparent and the adlayer contribution is dominant for the deposition mechanism. With our laser writing apparatus, we deposited 100 $\mu\text{m}$ , 3 $\mu\text{m}$  wide, and .03 $\mu\text{m}$  thick lines on a glass surface. In most cases they were well defined and exhibited a silver, reflecting surface. In addition, scanning electron microscopy showed these lines can exhibit the rippled surface morphology which has also been observed for indium and cadmium depositions. However, the electrical resistance of the aluminum lines was typically larger than 20 M $\Omega$ , corresponding to a resistivity value of at least  $10^6$  times that of the bulk material. Thus, despite its metallic appearance, the deposited material had low conductivity; nonetheless, the clear demonstration of a consistent, albeit low conductivity for laser written interconnects is an important step forward in laser writing technology.

Since use of trisobutylaluminum (TIBAl) produces better material in standard chemical vapor deposition (CVD) than TMAI, we also tried this compound. The vapor pressure of TIBAl is very low (0.5 Torr). We, therefore, had to use a flow-through system in order to be able to write 100 $\mu\text{m}$  long lines. The sample was heated to 100°C to assist in evaporating unwanted hydrocarbons from the CVD work. Again, however, we obtained the same results as described with the TMAI.

X-ray elemental analysis of the material deposited from both reactants revealed a high oxygen content. Quantitative analysis of lines written on an oxygen-free surface, typically tantalum, confirmed that the deposited material is very close to  $\text{Al}_2\text{O}_3$ . These results show that oxidation of the aluminum by gas-phase impurities is a major difficulty causing deposition of high resistivity aluminum. Note, however, that the photodeposition of Al in a chamber filled with a low pressure  $\text{O}_2$  background is a useful approach to direct writing of  $\text{Al}_2\text{O}_3$ .



Consider the reaction of atomic aluminum in an atmosphere of oxygen. In addition at an oxygen pressure of  $10^{-4}$  Torr the  $O_2$  imingment rate on the surface is in the same order as a typical photolytical deposition rate. At the vacuum levels used in our experiments ( $10^{-2}$  torr), the residual oxygen pressure is high enough to react immediately with the aluminum film. If high quality aluminum is to be deposited, it must be done at residual oxygen pressures below  $10^{-6}$  Torr. We are currently improving our vacuum system by building up a flowing system with a high vacuum capability of  $10^{-8}$  Torr, so as to improve the chances of writing high conductivity aluminum.

#### 4. Contact Formation on Aluminum

If laser direct writing of metals is to be used effectively for repair or customizing of integrated circuits, it must be compatible with the present processing technology, which is dominated by aluminum metallization. Subsequent laser processing to write interconnects on conventionally deposited aluminum metal runs is difficult because of the insulating  $Al_2O_3$  surface layer.

We studied various means of breaking through the aluminum oxide layer to provide a high quality electrical contact. The technique described here has been photodeposition of zinc with an in situ thermal drive in. Zinc was chosen because previous work has demonstrated that it can reduce aluminum oxide and that it is useful in a related scheme to etch aluminum locally .

Our method used two laser beams, a 257-nm UV beam used to photodissociate dimethylzinc (DMZn) and a 514-nm beam used to thermally drive in the zinc atoms. Both beams were focused onto an aluminum pad used to simulate an aluminum contact on an integrated circuit.

Our results to date have been successful but with limited yield. Good contacts with a resistivity of approximately  $10^{-5}$  ohm-cm<sup>2</sup> were sometimes formed

on one run, but under the same conditions the next run often displayed infinite resistance. We attributed these difficulties to the following two problems. The first involves the practical aspect of focusing two beams exactly on top of each other. Temperature calculations indicate that if the 514-nm beam is slightly out of focus or displaced from the 257-nm beam, the temperature necessary for diffusion will not be reached. The problem is compounded by the fact that increasing the power of the 514-nm beam can result easily in a shift of both the UV and green focal spots by heating up the optics in the optical train. Additionally, the UV beam is invisible except for a noticeable fluorescence at high power.

A second, more difficult problem is connected to the relative rate of deposition versus that of surface heating. If the photodeposition of zinc is significantly faster than the process of zinc indiffusion, then the surface optical properties and hence temperature will change prior to alloying of the zinc. As a result, the process window is very narrow, bracketed on one side, for example, by insufficient incorporation and on the other by film ablation.

Because of these results, began a systematic study of zinc deposition to determine the optimum deposition rates and surface temperature. The study included UV spectroscopic measurements of diethylzinc (DEZn) gas and adsorbed, and a parametric investigation of the deposition rate. The results of this study are given in Section IIC., below.

### C. Application of Photodeposition

In addition to the aluminum deposition work, a parallel effort in applications of direct writing was begun. With DMCD, photodeposited cadmium lines were used to simulate a IC chip repair on a test chip. The ability to bypass a defective MOSFET as well as the ability to join severed metal lines was demonstrated as shown in Fig. 2. Note that the measured resistivity of these IC interconnects

is higher than the 4-times bulk resistivity exhibited for cadmium lines themselves. The decreased conductivity results from the contact- or interface - resistance between the deposited cadmium and the existing aluminum connector. Because these chips have been exposed to air, the Al lines are covered with a thin layer of  $\text{Al}_2\text{O}_3$ . The Cd lines are, in fact, in intimate contact with the aluminum oxide and not with the pure metal. A method of improving this interface structure was discussed above in Section II.B.4.

This project on LSI circuit repair was based on discussions with engineers at ITT Shelton, Conn. They have a continuing need for repair and reconfiguration capability in their chip testing cycle. The UV photodeposition technique which we are pursuing here provides an excellent tool for this application.

#### D. Deposition of Refractory Metals

##### 1. Deposition of Tungsten

We chose to begin our investigation of refractory metal deposition, with photodeposition using 257-nm radiation from the frequency-doubled, argon-ion laser. The initial parent gas for deposition of tungsten was  $\text{WF}_6$  in a  $\text{H}_2$  background gas. A very slow deposition rate ( $10^{-8}$ ) of the metal was measured for this mixture. This deposition rate results from the low absorption coefficient of the tungsten hexafluoride at this wavelength. The deposited metal is of low quality since it has a very high resistivity and low mechanical strength. Since the doubled- $\text{Ar}^+$  laser output power and, therefore the power density on the sample surface, is limited, we chose to use 350-nm laser light. Note that  $\text{WF}_6$  has an even smaller absorption coefficient at this wavelength. Despite this, the deposition rate was improved, undoubtedly due to the onset of thermodeposition. However, the line resistivity was still more than  $10^6$  times the bulk value and the surrounding sample surface was damaged by the hydrofluoric acid generated in the

reaction zone.

Another tungsten compound which can be used for laser-induced writing is tungsten hexacarbonyl, which is a solid at room temperature and has a vapor pressure of 0.1 Torr. The optical absorption coefficient at 257 nm is very high, which allows deposition even at this low pressure. However, at 350 nm it is known from the literature that this compound needs more than one photon to release the metal atom. Thus higher laser powers are required from deposition for 350 nm than 257 nm. For example, the optimal power density for indium from trimethylindium, which also requires only one photon to photodissociate, is on the order of 1-10 kW/cm<sup>2</sup>.

Our experiments were done with the reactant at room temperature and the sample substrate heated, in order to adjust the adlayer thickness and gas pressure. During the deposition, the cell was connected to a roughing pump to remove the carbon monoxide photoproducts continually. At 400 - 1000 kW/cm<sup>2</sup> or 30-75 mW incident power with the 350 - 360 nm laser light, the deposited lines, which were 3- $\mu$ m wide and 100 - .200  $\mu$ m long, exhibited a resistivity of 1-2 times the bulk. The deposition rate is on the order of 100 Å/s. We believe that the deposition process at this power level is no longer purely photolytical. The induced temperature during irradiation is estimated to be between 300 and 700°C, since no obvious damaging of the glass was observed. The temperature is high enough to cure the metal (400°C) and to form low-resistivity tungsten. This is the first demonstration of this "hybrid" type of deposition mechanism; it offers the possibility of initiating the deposition process on a transparent substrate, and yet allowing curing the of material during processing.

The technique is termed hybrid since it uses both photolytical and pyrolytical fragmentation of the reactants. At the time of our earlier studies, the detailed mechanism was not very well understood. For a transparent substrate, the presence of an initial, photolytically deposited film is a very important factor in

hybrid deposition since this film causes sufficient temperature rise to allow subsequent thermal processing.

In order to investigate the characteristic parameters of this film, we performed reflectivity measurements during the tungsten deposition on sapphire. This type of measurement provides another method of probing the temporal changes in the optical properties of the surface. The measured reflection coefficient increases in the high and medium power regime from 8% at the start of the exposure to a maximum value of 25% after roughly 1 to 5 seconds. In the low power regime, however, an initial decrease of the reflected intensity and an increase afterwards were observed. A comparison of these measurements with model calculations makes possible an estimation of the refractive index of the initially grown film. The results show that the film must have a real part of the index of refraction close to that of sapphire. The imaginary part of the film's index can be calculated to be in the range of 0.02 to 0.1. This complex index of refraction is not typical for a metallic tungsten film. Instead, it is more representative of a refractive index of an organic film, e.g., a stabilized, tungsten-carbonyl compound. Similar experiments were performed on Si, Al (on silicon), GaAs and glass substrate material. The observations on all of these materials confirm the presence of the photodeposited adlayer, which initiates the subsequent pyrolytical heating and this allows the process to take place at relatively low powers even in transparent substrates.

## 2. Deposition of Molybdenum from $\text{Mo(CO)}_6$

Figure 3 shows the measured resistivity ratio as a function of the incident laser power for molybdenum deposition on glass and GaAs. For slow scan rates, i.e. 1  $\mu\text{m/s}$ , the resistivity ratio decreases rapidly with power until the line resistivity levels off at roughly 100 to 300 times the bulk value. The lines



hybrid deposition since this film causes sufficient temperature rise to allow subsequent thermal processing.

In order to investigate the characteristic parameters of this film, we performed reflectivity measurements during the tungsten deposition on sapphire. This type of measurement provides another method of probing the temporal changes in the optical properties of the surface. The measured reflection coefficient increases in the high and medium power regime from 8% at the start of the exposure to a maximum value of 25% after roughly 1 to 5 seconds. In the low power regime, however, an initial decrease of the reflected intensity and an increase afterwards were observed. A comparison of these measurements with model calculations makes possible an estimation of the refractive index of the initially grown film. The results show that the film must have a real part of the index of refraction close to that of sapphire. The imaginary part of the film's index can be calculated to be in the range of 0.02 to 0.1. This complex index of refraction is not typical for a metallic tungsten film. Instead, it is more representative of a refractive index of an organic film, e.g., a stabilized, tungsten-carbonyl compound. Similar experiments were performed on Si, Al (on silicon), GaAs and glass substrate material. The observations on all of these materials confirm the presence of the photodeposited adlayer, which initiates the subsequent pyrolytical heating and this allows the process to take place at relatively low powers even in transparent substrates.

## 2. Deposition of Molybdenum from $\text{Mo}(\text{CO})_6$

Figure 3a shows the measured resistivity ratio as a function of the incident laser power for molybdenum deposition on glass and GaAs. For slow scan rates, i.e. 1  $\mu\text{m/s}$ , the resistivity ratio decreases rapidly with power until the line resistivity levels off at roughly 100 to 300 times the bulk value. The lines

deposited on glass under these conditions appeared black, discolored on the edges in the optical microscope and were very brittle under mechanical stress. We believe, under these process conditions, the surface temperature rise is too high and leads to undesirable secondary reactions such as the cracking of CO ligands at the metal surface. This effect, in turn, gives rise to the formation of carbon or carbonyl inclusions. On glass, the resistivity ratio could be improved by increasing the writing speed.

At high writing rates, i.e. 25  $\mu\text{m/s}$ , shiny silver metal lines with electrical resistivities of 7-10 times the bulk values were obtained. At these scan rates, the surface temperature is just sufficient to cure the deposits to achieve good resistivity but not enough to induce a predominant thermochemical processing.

The corresponding line thickness for the 1  $\mu\text{m/s}$  writing speed is shown in Fig. 3b for the same two substrates. As can be seen, above 15 mW, the growth rate on glass is much faster than on GaAs. This fast growth on glass is attributed to the higher-temperature rise on the glass surface due to the low thermal conductivity. The deposition process on glass is probably dominated by the thermochemical decomposition at incident laser power levels above 15 mW. However, we believe that the processing is always initiated by a photolytic film deposition. The exact ratio of photochemical to thermochemical processing under these conditions is at present unknown.

#### E. Detailed Investigation of Processes Occurring in Deposition of DeZn, to Provide a Specific Theory of Photodeposition

Laser photodeposition is complicated by the fact that photodeposition can occur both from the gas and surface-adsorbed molecular phases. Fortunately, as long as the laser-driven growth is sufficiently slow that neither process depletes their respective molecular phases, the photodeposition rate from each process can be

treated separately. The total deposition rate is then obtained by superimposing the rates of each phase.

Consider first the deposition from the gas phase. Several factors must be considered in modeling deposition from this phase. In addition to the obvious variables such as laser power, precursor concentration, optical cross-section, and photodissociation efficiency, one must also take into account laser polarization effects, the metal-atom velocity distribution, surface sticking coefficient, mean free path length, metal atom lifetime, and gas phase nucleation. To solve this problem rigorously for the general case, one must solve the Boltzmann transport equation, which is extremely difficult even if all of the system parameters described above were known. However, analytic solutions can be found if we consider deposition in both the diffusive (high pressure) and ballistic (low pressure) limits, and if we make reasonable simplifying assumptions regarding the deposition physics.

At high total gas pressures in the cell, the mean free path length of the photogenerated metal atoms will be short compared to the radius of the focused laser,  $w_0$ . The velocities of the generated metal atoms are quickly randomized and reach thermal equilibrium well within the focused beam. The Boltzmann transport equation then simplifies to the diffusion equation. Most of our measurements were performed by writing thick metallic lines at a slow scan speed. In this case, the dwell time for each pixel is long compared to the diffusion time to the surface and the system can be assumed to be in steady state. Furthermore, since for these high gas pressures, the probability to contribute to the deposition process is very low for species formed far away from the substrate, the focused laser beam can be approximated by a cylindrical beam geometry. The surface sticking coefficient is included in a boundary condition on the total flux to the surface. This problem is analagous, for example, to that of surface recombination used in solid state device

physics. This boundary condition at  $z=0$  is given by

$$(1) \quad \frac{dN(r, 0)}{dz} = \frac{\alpha v N(r, 0)}{D}$$

where  $D$  is the diffusivity,  $N$  is the metal atom concentration,  $v$  is the metal atom velocity,  $\alpha$  is the sticking coefficient and the coordinate system is shown in Fig. 4. The steady state diffusion equation for two dimensions can be solved with the aid of a Hankel transform and by noting that the deposition rate is the diffusivity times the metal-atom concentration gradient. The rate of deposition is then

$$(2) \quad R_D(r_0) = \frac{P\sigma n}{2\pi h\nu} \int_0^\infty dk \exp\left(-\frac{k^2 w_0^2}{8}\right) J_0(r_0 k) \frac{k (3\alpha/\lambda)}{\sqrt{k^2 + 1/\tau D} (3\alpha/\lambda + \sqrt{k^2 + 1/\tau D})}$$

where  $P$  is the incident laser power,  $\sigma$  is the gas phase cross-section,  $n$  is the reagent-gas concentration,  $\lambda$  is the mean free path length,  $r_0$  is the distance along the surface from the beam center,  $\tau$  is the lifetime of the metal atom before a scavenging gas-phase reaction, and  $k$  is the inverse of the variable. An important point regarding Eq. 2 is that it is not a strong function of the diffusivity, and therefore, the deposition rate should be independent of buffer gas pressure.

An analytic expression for deposition at the center of the beam,  $r_0=0$ , can be obtained from Eq. 2 by assuming a long atom lifetime and a uniform sticking coefficient of 1, over the entire substrate surface. Then,

$$(3) \quad R_D(0) = \frac{P\sigma n}{\sqrt{2\pi} h\nu w_0}$$

The sticking coefficient of zinc atoms on freshly deposited zinc is approximately 1 but on a quartz surface it is at least two orders of magnitude lower. This assumption of  $\alpha = 1$  is appropriate for deposition in the vicinity of  $r_0=0$  as long as there is a fully developed zinc deposit and the mean free path is much less than  $w_0$ . The assumption of a very long, gas-phase lifetime is valid for zinc and other Group IIB metals. Since gas-phase nucleation requires a  $\sim 10$  atom cluster, the

atom lifetimes are expected to be on the order of hundreds of milliseconds or greater.

For the case of a diluted gas, i.e., very low pressure, the metal atom mean-free-path length is large. In this case, a metal atom will move undeflected from the beam; if it hits the deposit, it will either stick or scatter, with little chance of returning to the deposit. The Boltzmann transport equation then simplifies to that for ballistic streaming. Despite the fact that the transport equation is of a different form, a simple continuity consideration shows that for certain conditions the steady-state atom flux arriving at the surface is identical to the diffusion-limited case. In particular, this conclusion is valid for  $r_0=0$  if  $\tau \approx 1$  over a region of comparable size to the laser beam and if  $\tau$  is long assumptions which are valid for our experiments. This ballistic case has been presented by Wood et al.

Photodeposition from the adlayers is considerably simpler than from the gas phase since the metal atoms are released at the solid surface. Just as for the case of gas-phase photolysis, surface-phase deposition requires that the adsorbed layer must be continuously replenished. However, under our conditions of low laser power and small spot size, this process is not a rate-limiting step since reagent molecules diffuse to the reaction zone from the hemisphere above it at a rate faster than the rate of photodecomposition. Assuming simple linear photodissociation, the expression for the deposition rate from adlayers is then

$$(4) \quad R_s(r_0) = \frac{2PA \exp(-r_0^2/w_0^2) E}{h\nu \pi w_0^2}$$

where  $A$  is the optical absorption by the adsorbed molecules and  $E$  is an enhancement factor which may be due to a variety of factors including an enhancement of the local optical field in the vicinity of metal features, or the photochemical yield on



the solid surface. Rigorously, as the deposit thickness increases,  $E$  will slowly change through the thickness-dependent film morphology and material properties.

Equation 4 exhibits an important temperature dependence which stems from the temperature-dependent coverage and, hence, optical absorption of the physisorbed layer. The coverage directly affects the optical absorption of the physisorbed layer, given by

$$(5a) \quad A = \frac{A_0 C p}{(p_0 - p) [1 + (C-1)p/p_0]}$$

$$(5b) \quad A \approx \frac{A_0 C p}{p_0}$$

where  $A_0$  is the optical absorption of a uniform monolayer,  $p_0$  is the vapor pressure at the temperature of the substrate and  $C$  is a constant, which is specific to a particular molecule-substrate system. The dominant temperature dependence comes from the Arrhenius factor in the saturated vapor pressure  $p_0$ . Inserting the temperature-dependent vapor pressure of DEZn into Eq. 5b, gives an expression for the adlayer absorption,  $A$ , which exhibits an exponential dependence on  $1/T$ .

$$(6) \quad A \approx \frac{A_0 C p \cdot 10^{2000/T}}{10^8}$$

Since the surface deposition rate is directly proportional to the optical absorption, it will exhibit a similar temperature dependence.

As seen above in Eq. 3 and 4, photodeposition has a different dependence on the experimental parameters for writing, depending on whether dissociation occurs in the gas or surface phase. As a result, it is useful to consider a ratio of the two rates to show under which experimental conditions a particular molecular phase is the dominant contributor to the writing process. In particular, the ratio of

surface to gas-phase deposition rates at beam center,  $r_0=0$ , is  $R_s/R_c = \frac{4AE}{n\sigma\omega_0\sqrt{2\pi}}$  (7).

For conditions typical for this experiment, i.e.  $A=0.0015$ ,  $w_0 = 3\mu\text{m}$ ,  $n=1.6 \times 10^{17}/\text{cm}^3$  ( $\sim 5$  Torr),  $\sigma=0.03\text{\AA}^2$ , and  $T=20^\circ\text{C}$ , we find the surface deposition rate at room temperature to be approximately 30 times as fast as the gas-phase deposition rate. In doing this calculation, we have assumed for simplicity that  $E=1$ . As a result of the  $(w_0)^{-1}$  dependence of this ratio, surface-phase deposition will dominate for small spot sizes. This effect can be ultimately shown to be due to geometrical spreading for atoms generated in the gas column at  $z > w_0$ . For pressures low compared to  $p_0$ , both  $A$  and  $n$  are linearly dependent on pressure and the ratio is independent of gas pressure. For fixed temperatures, adlayer deposition will dominate for small spot sizes. In addition, surface-phase absorption has an approximately exponential dependence on temperature, through  $p_0$ , whereas gas-phase deposition has only a weaker inverse temperature, through the gas-phase density. As a result, surface deposition will dominate for low substrate temperatures.

Our experimental data show clearly that the dominant phase contributing to the deposition can be changed by the substrate temperature. Equations 3 and 4 show that the deposition rate has a different dependence on spot size for gas and adlayer deposition, respectively. For a purely gas-phase-dominated mechanism, the slope, when plotted on log-log axes, should be 1, while in an adlayer dominated case the slope should be 2. Wood, et al. had earlier shown that for the case of deposition from dimethyl cadmium at  $20^\circ\text{C}$ , the deposition was dominantly from the gas phase - at least for spot sizes  $> 20 \mu\text{m}$ . In Fig. 5, we plot the time to the  $1/e$  transmission point versus the laser spot diameter for substrate temperatures of  $20^\circ\text{C}$  and  $70^\circ\text{C}$ . The time to the  $1/e$  transmission point is obtained by using a stationary beam and measuring the transmitted light as described earlier. These measurements were performed on sapphire substrates with an incident laser power of

0.07mW. In doing these experiments, care must be taken to prevent laser induced substrate heating which can alter the resulting slopes. We show for DEZn that either adlayer or gas-phase dominated deposition can be seen, depending on the substrate temperature. At 70°C, the deposition mechanism is dominated by gas-phase photodeposition, as shown by the slope of 1 in Fig. 5. At 25°C, where the slope of Fig. 5 is 2 for small spot sizes and approaching 1 for larger spot sizes, the deposition scheme consist of a primarily adlayer deposition for smaller spot sizes and a dominantly gas phase deposition for larger spot sizes. The change in the dominant deposition scheme that produces the change in slope of Fig. 5 can be seen from Eq. 7. At a spot size of 3.6  $\mu\text{m}$ , the calculated surface phase deposition rate is 25 times faster than the gas phase deposition rate. Alternatively, at a spot size of 120  $\mu\text{m}$ , the gas phase deposition rate is 1.2 times faster than the surface phase deposition rate. The calculated changeover point from surface dominated to gas-phase-dominated deposition should occur when the ratio of surface to gas phase deposition (Eq. 7) equals 1, i.e., when the spot size equals  $\sim 50$   $\mu\text{m}$ . Our experimentally determined changeover point occurs near 25  $\mu\text{m}$ . To first order, this spot size is in good agreement with the calculated spot size. The discrepancy can be due to a different adlayer absorption on sapphire than on quartz. The difference in the deposition rates between the gas-phase-dominated deposition at 70°C and the gas-phase-dominated deposition at 25°C and large spot sizes can be attributed to increased surface nucleation at the lower substrate temperature. The changeover from adlayer to gas phase again reflects the fact that for higher substrate temperatures, the adlayer coverage decreases. This observation is in good agreement with the data presented in Fig. 5 and further confirms the adlayer-dominated nature of the deposition mechanism at room temperature.

### III. DIRECT FABRICATION OF DIFFRACTION GRATINGS

#### A. Growth of Submicrometer Gratings

##### 1. Resonant Growth of Metal Gratings

We have used the interference of two UV-laser beams at the window inside of the gas cell, to produce a high quality metal grating by photodissociation of adsorbed metal-alkyl molecules. We have now found that at a specific series of grating spacings, the growth rate of the gratings is greatly enhanced. The phenomena can be interpreted as an additional optical-enhanced growth rate, induced by the constructive interference of the reradiated electromagnetic fields of the individual deposited metal strips. Such resonance phenomena clearly are an important consideration in the use of laser-assisted processing. In addition, the maskless growth of submicrometer gratings has applicability to holographic storage of data and fabrication for optical electronics.

The experiments were performed with a 257-nm ultraviolet radiation from a frequency-doubled, argon-ion laser. The laser was split into two beams and then combined to make an interference pattern on the inside of the entrance window of an optical cell, which was filled with the metallorganic gas. The polarization of the electric-field of the ultraviolet beams was parallel to the grating grooves. By varying the incident angles of the two beams with respect to the window surface, the spacing of the interference pattern could be adjusted. Since the two beams travel in the window material and the grating is created in the window-adlayer-gas interface layer, the grating formation is strongly influenced by the choice of the window material and the optical parameters of the metallorganic gas. Two different window materials (quartz,  $n=1.50$  and sapphire,  $n=1.84$  at 254 nm) and two different metal-alkyls (dimethylcadmium DMCD and Diethylcadmium DECD) were used.

Under these particular deposition conditions, the photodeposited metal grows preferentially from the adsorbed layer. The typical laser power density was 6 mW over an area of  $1/3\text{cm}^2$ . Metal gratings with spacings 0.4 to  $0.9\mu\text{m}$  were

obtained with a typical growth times from 10 seconds to 2 minutes depending on whether or not resonance growth occurred. The grating formation was investigated by measuring the temporal variation of the intensity of the minus-first-order diffracted He-Ne laser beam at 632nm.

We measured the time interval over which the intensity of the diffracted beam increased from 20 to 80% of the maximum value. This portion of the growth curve was approximately linear and the inverse of this time was taken as the speed of growth. It was found that the growth rate depended sharply and periodically on the spacing of the grating. This behavior was found for both window materials and for both photoreactive gases. The resonance conditions as measured from this data could be fitted with the expression:

$$a_n = (m+1) \lambda_0 / 2n$$

where  $\lambda_0$  is the vacuum wavelength,  $n$  the index of refraction of the window material, and  $m$  is an integer.

Fig. 6. shows the two resonance peaks for  $m=3,4$ , which were observed for quartz and DECD, between 0.4 and 0.7 $\mu$ m. In Fig. 6. the two corresponding resonance peaks between 0.4 and 0.65  $\mu$ m, observed for sapphire and DECD, are depicted. This window material causes a substantial shift toward shorter grating space, with respect to the results with the quartz. The scanning electron microscope photographs of the gratings in the early stage of the growth revealed a granular structure. In particular the metallized regions consisted of a random distribution of nearly-spherical metal particles with  $\lambda_0/2n$  diameter.

The essential physics of the resonant growth can be explained by a simple model in which the UV light interacts with an array of rough strips with time-dependent thickness and width. Once metal strips start to form along the



maxima of interference pattern, oscillating currents are induced and supported by the granularity of the deposited structure. Those currents, in turns, emit radiation like an antenna array. The total optical field acting on each strip is the sum of the incident optical field and the reradiated field from all other strips. A resonance takes place when each of the components of the optical fields on the strip are in phase. Since the incident field of two neighboring strips have opposite phase, the induced currents in the even- or odd-numbered strips are also opposite. The retardation of the reradiated field requires that for in-phase overlapping with the excitation field, that the spacing between adjacent strips has to be an odd number of  $\lambda_0/2n$ .

An accurate theoretical model for the process based on calculating the reradiated field using Maxwell's equations has been developed on a separate ARO contract.

## 2. Fabrication of Deep, Ultrahigh-Aspect-Ratio, Diffraction Gratings

We have learned that the unusual etching which can be obtained with liquid phase etching using 257 nm light can be used to create a variety of microfabricated features. These features include trenches and micrometer period diffracton gratings. In a different set of experiments, using this technique we have etched arrays of deep micrometer-size grating grooves with a projected interference pattern. Rapid ultraviolet etching has enabled us to etch high-aspect gratings with a maximum depth-to-spacing ratio of 20. As in the focused beam experiments described below, the etched structure acts as a waveguide which confines and efficiently transmits the processing beam.

### B. Direct Fabrication of Optical Structures

#### 1. Light-Guided Microfabrication

We have examined UV-induced wet etching of GaAs for fabrication of novel electrooptical structures. The deep UV wavelength initiates a different and more rapid interface chemistry than similar etching at visible wavelengths. The etching rate at very low laser powers is sufficiently fast to make very deep vertical features without heating the solution or damaging the substrate surface.

As a result of the changed chemistry, all doping types of GaAs can be readily etched in a wide variety of etching solutions. We have etched n, p, and semiinsulating (100) GaAs with the frequency-doubled  $\text{Ar}^+$  laser in three different solutions ( $\text{H}_2\text{O}_2$  with  $\text{H}_2\text{SO}_4$ ,  $\text{HNO}_3$ , and  $\text{KOH}$ ). A typical etch rate is  $10 \mu\text{m}/\text{min}$  for a power density of  $200 \text{ mW}/\text{cm}^2$  and a spot of  $10 \mu\text{m}$  diameter. This is a factor of 30 times greater than the rate for etching with visible light under the same conditions. This enhancement cannot be explained by the light absorption in the liquid nor by the change in the carrier concentration on the GaAs surface due to the shorier absorption length. We attribute this increased etching rate to nonthermalised holes (hot holes) created by the UV photons. These hot holes are able to activate a different chemical process. Separate experiments proved that even pure water oxidizes the GaAs surface under deep UV irradiation.

Another difference between the etching with UV light compared with visible light is the well resolved and highly directed etching during UV irradiation. By focusing the laser beam to a  $3\text{-}\mu\text{m}$  spot, we were able to drill via-holes through a  $250 \mu\text{m}$  wafer with perfect vertical walls, as shown in Fig. 7. Fig. 7 shows that the surrounding area of the surface hole is almost undamaged. The directed etching can be attributed to a waveguiding effect. In the deep UV region, GaAs behaves like a metal. During the formation of the hole the incident light is guided inside the hole as it would be in a hollow metallic waveguide. This effect keeps the walls

straight and smooth. At UV intensities above  $\sim \text{kW/cm}^2$ , scattered light inside the hole destroys the vertical walls and prevents further penetration. For visible light, we were not able to drill holes with such high aspect ratios. For the visible wavelength range the reflectivity is dominated by the high index of refraction and the waveguiding effect is much lower.

Fig. 8a shows typical profiles of via holes and slits etched through the GaAs wafer. The slits were etched by scanning the wafer perpendicular to the axis of the laser beam. In all experiments, the laser beam was focused such that the beam waist was on the front of the semiconductor wafer. The entrance and the exit of the etched structures are well defined and the surrounding area is undisturbed. Another characteristic of these etchings is their smooth and vertical side walls. The etched width, typically 2-3  $\mu\text{m}$ , remains constant, independent of the etched depth. In contrast to this, a focused laser beam with a 3- $\mu\text{m}$  waist diverges considerably over the corresponding distance, as shown in Fig. 8b. The measured confocal beam parameter is only 30  $\mu\text{m}$  as compared, for example, to the perfectly vertical etch through the 200- $\mu\text{m}$ -thick wafer. This clearly shows that the processing beam is confined inside the hollow, etched structure and prevents the beam from diverging. In addition, the characteristically high reflectivity of GaAs in the ultraviolet efficiently guides the laser beam inside the etched feature.

Most of our experiments were performed on single-crystalline (100) GaAs, doped with Si ( $n=10^{18} \text{ cm}^{-3}$ ). The samples were of different thicknesses which ranged from 40  $\mu\text{m}$  to 250  $\mu\text{m}$ . In addition, three different crystallographic orientations of GaAs crystals, (111)A, (111)B, and (110), were briefly examined for the sake of comparison. The etchant was a diluted  $\text{HNO}_3$  aqueous solution (1:20 by volume). This solution has no dark etching and only weakly absorbs ultraviolet light. This solution, in conjunction with the ultraviolet illumination, allows efficient etching of all doping types of GaAs. In addition to the experiments with

GaAs, we have studied light-guiding in Si and InP using aqueous HF and HCl solutions (both 1:20 by volume), respectively. Since these materials have very similar optical properties to GaAs at 257 nm, the waveguiding in the etched structures is efficient and similar to that seen in GaAs crystals.

The possibility that the vertical etching relies on the semiconductor crystal anisotropy was ruled out after the experiments with GaAs samples with different crystallographic orientations. A weak crystallographic dependence was found, resulting in average etch rates of 7 : 9 : 9 : 11  $\mu\text{m}/\text{min}$ . for the (111)A, (100), (110), and (111)B faces, respectively. However, perfectly vertical holes are obtained for all etching of vertical high-aspect profiles in all crystallographic directions.

In order to determine a mechanism for the formation of vertical waveguides, we monitored the development of holes, as shown in Fig. 9. The vertical cross section of the etched feature was measured and compared with the Gaussian intensity profile of the laser beam. Initially, the etch profile is essentially identical to that of the incident laser beam, as shown in Fig. 9. However, as the etch depth increases, the feature assumes a tubular, non-Gaussian profile, Fig. 9. The initial formation of the non-Gaussian shape can be explained by a simple ray-optics approach coupled with the linear intensity-dependent etch rate. This model includes the angular-dependence of the local absorbed light intensity on the tilt of the etched surface.

In fact, much of the speed and anisotropy of the etching can be attributed to the formation of these efficient hollow, optical waveguides. We have characterized these guides by measuring the optical loss and the field distribution within the guide for GaAs samples of different thicknesses. The measured data, shown in Fig. 10, are in good agreement with the theoretical considerations, outlined below. In general, the optical loss is small, even for 200 to 300- $\mu\text{m}$

thick samples, and does not significantly limit the etch rate.

The power loss during propagation of the laser beam through the hole is due to the "leaky" nature of the guide. Such circular hollow dielectric and metallic waveguides have been thoroughly discussed previously. Using this treatment, we consider a hollow semiconductor cylinder of radius  $r$  with an inner transparent, aqueous medium of the refractive index of 1.33. The complex GaAs refractive index,  $n$ , has a strong wavelength dependence through the visible and ultraviolet region. For example,  $n = 4.29 + i0.36$  and  $2.65 + i3.37$  at  $\lambda = 514$  nm and 257 nm, respectively. The number of confined modes that can be supported by the waveguide depends on the value of  $r/\lambda$ . Typical values for  $r/\lambda$  obtained in our experiments are large enough to allow a multi-mode operation. However, for the linearly polarized incident fields, the hybrid modes ( $EH_{nm}$ ) are preferentially excited. In particular, the  $EH_{11}$  mode matches closely with the  $TEM_{00}$  free-space laser mode. This was experimentally confirmed by measuring the optical field transmitted through the etched bores of different lengths. In all cases, the guided laser beam retains the initial linear polarization. The projected far-field pattern, which gives a measure of the field distribution within the guide, shows a distinct central intensity lobe, characteristic for the  $EH_{11}$  mode. In addition, according to the theory of Marcatili and Schmeltzer, the attenuation coefficient of  $EH_{11}$  mode,  $\alpha_{11}$ , is proportional to the ratio  $\lambda^2/r^3$ . The same dependence is obtained in experiments with different waveguide radii and two laser wavelengths, shown in Fig. 10. For example, the 514-nm light has a higher attenuation coefficient than the 257-nm light. Note that the different radii can be obtained by varying the incident beam intensity.

#### b. Aqueous Etching of Semiconductors Using Pulsed Ultraviolet Lasers

The central characteristic of this light guided etching process is its



fast, directional etching, resulting in deep perfectly vertical structures. This highly directional and rapid etching is also observed for other semiconductors, e.g. Si and InP. The same distinct performance of the ultraviolet light was also confirmed in projection illumination of GaAs using a cw laser. Very deep, submicrometer-wide grooves were produced over an area of  $0.5 \text{ cm}^2$  by projecting a light pattern onto the semiconductor surface.

However, for wafer-scale, parallel processing, no available cw, ultraviolet source produces enough light to provide the necessary intensities. A powerful light source in this wavelength region is a pulsed, excimer laser, e.g. the KrF laser at 248nm. Here we report, for the first time, the use of a pulse, UV laser in wet etching. Further, we show that the light-guided projection imaging may be accomplished.

The experimental setup used a repetitively pulsed (1-100 Hz) KrF laser at 249nm; although ArF (193 nm) and XeF (351 nm) lasers were also briefly examined for the sake of comparison. The laser output was passed through a mask and was imaged with a 70-mm focal-length lens onto the semiconductor surface, as shown in Fig. 11. The masks were typically either slits or a simple array of square holes. The laser was mounted on a vibration isolation platform to eliminate blurring due to sample movement. Calibrated attenuators were used to vary the laser power.

All three doping types of gallium-arsenide (n, p and semiinsulating crystals) were examined. The GaAs substrate is mounted inside a quartz cell filled with an aqueous solution. The etched profiles were determined by optical and electron microscopy and surface probing. For the pulse peak power densities ( $1.5 \text{ mW/cm}^2$ ) used in our experiments, we could not find either laser damage of the semiconductor surface or excessive heating of the solution. Generally, the etched structures were well-defined and with a smooth morphology.

A 5%  $\text{HNO}_3$  mixture was chosen as the etching solution because it has no

perceptible etching outside the illuminated region for all wavelengths, from visible to ultraviolet. It does, however, have optical absorption in the ultraviolet (below 300 nm) which is proportional to the amount of  $\text{HNO}_3$  in solution.

The slower etching performance of the excimer laser at the lower laser intensity is attributed to a limitation of the laser-induced carrier density in the GaAs. For example, pulse-power densities above  $10 \text{ kW/cm}^2$  induces a high transient carrier concentration. Then, a very fast carrier-recombination mechanism, like stimulated emission or Auger recombination will become effective and will decrease the carrier lifetime. As a result, for the pulse intensities performed in our experiments the available hole-concentration on the surface will not increase linearly with the photon flux.

The relative etching of n, p, and seminsulating GaAs are given in Table I. These rates are considerably different from the ones seen for visible light induced etching of GaAs. They are, however, nearly identical to those observed for very low power, cw etching. In that case, the high etching rate of the semiinsulating and p-type materials was attributed to the short absorption depth of the ultraviolet light, and the consequent ejection of nonthermalized photogenerated holes.

Projection etching of GaAs was done for both 4:1 and 1:1 imaging geometries. As electron-microscope micrograph of the sample with 4:1 imaging is shown in Fig. 12. Note that the edges of the etched region are smooth, but sharply defined. The internal profile of the etched holes is tapered for a distance of about one diameter of the hole into the sample. This tapering is a result of light guiding in the etched feature. After etching one diameter into the sample, the tapering ceases and the diameter remains constant.

### 3. Theory of Light Guided Etching

To provide insight to the initial stages of light induced etching, we

introduced a simple, numerical simulation of the etching process. The model is based on a ray optics approach, which is valid because diffraction effects are not dominant for the widths, depths, and the wavelength considered here. The model includes the angular-dependent reflectivity (derived from a modified version of the Fresnel equations), absorbed, surface- power density, and etching directionality. Since the shape and incident angle change during etching, these terms change as the hole evolves. The model takes into account not only the etching of the incident light (first strike), but also the etching of the first internal reflected light (second strike) of the incident beam off the walls to another portion of the hole. Fig. 13 shows the result of the model calculating a 10- $\mu\text{m}$ -deep hole. The two depicted curves compare a calculation which considers only the first strike of light rays, with the results which include the second strike. We found that the second strike is predominantly responsible for the vertical wall formation and allows the via to form. We therefore were able to conclude that the surface angular tilt also plays an important function in changing the power absorption and etching directionality of the via.

#### 4. Silicon Etching

We have investigated laser-enhanced, wet etching of silicon. Typically, wet etching of silicon is accomplished using an oxidizing agent and a fluorinating solvent such as  $\text{HNO}_3$  and  $\text{HF}$ , respectively, in a water solution. However, as a result of our experiments in GaAs using UV light, we were led to believe that in the presence of UV light,  $\text{H}_2\text{O}$  alone would oxidize the silicon. As a result, we eliminated the chemical oxidizer and instead used only focused laser irradiation with a silicon sample immersed in a diluted aqueous  $\text{HF}$  solution.

We have thus far studied the etching effect of a 257 nm source obtained from a frequency-doubled cw  $\text{Ar}^+$  laser on silicon samples, which were n-type with  $\langle 100 \rangle$

orientation and 3 ohm-cm resistivity. Solutions of 5, 10, and 20% HF in H<sub>2</sub>O were used and etch rates, resulting from incident power levels ranging from 10 to 10<sup>4</sup>W/cm<sup>2</sup>, were measured. The incident laser beam was focused onto the silicon surface, which was covered with a HF solution and a thin quartz window. The solution was thus a nonflowing system. The sample was scanned slowly normal to the incident beam in order to etch grooves. The etch depth was measured by cleaving the etched grooves and photographing them in a scanning electron microscope. Etch rates as high as 16  $\mu$ m/min are reported for a 10% HF solution at 8.5 kW/cm<sup>2</sup> (Fig. 14). Furthermore, it was demonstrated that high-aspect-ratio holes as well as vias could be etched with this technique, creating features on the order of 5 to 10  $\mu$ m in diameter and as deep as 100  $\mu$ m. In all of these experiments, we sought to maintain well-defined features with minimal damage to the surrounding areas and smooth sidewalls. Higher etch rates were recorded using higher power or a more concentrated solution; however, these conditions resulted in significant damage to surrounding regions and were thus not studied further.

We can safely deduce that one of the mechanisms involved in achieving such high-aspect-ratios is a waveguiding effect of the incident laser beam down the length of the etched hole, as was observed in previous work for the etching of gallium arsenide. The etching mechanism itself must be due to a photooxidizing sequence by the UV beam of the silicon, in which the oxide is subsequently removed by the HF.

##### 5. Waveguided Etching of InP

We have performed preliminary experimental work to characterize the photochemical etching process of InP. The motivation for developing etching techniques for this material is that InP and InP-based alloy are used extensively in

electrooptical devices. New etching techniques can lead to novel, integrated, electrooptical components such as through-wafer waveguides, controllable profile deep gratings, and optical fiber interconnects.

Previously published work regarding laser-induced aqueous etching of InP dealt with using visible laser light coupled with and without external biasing. We report on the use of deep-ultraviolet, laser-induced aqueous etching of bulk (100) n-type InP without the use of external electrodes. The etching is rapid, directional, and results in high-aspect features. The theoretical and experimental formation of via holes in this material, is similar to the GaAs hole formation we reported on this subject in the previous report.

This etching process, in which we believe nonthermalized holes give rise to an enhanced oxidation-reduciton reaction, has been previously reported for GaAs of varying doping types (n, p, and SI type). In comparison, InP proved to be slightly slower than GaAs in its etch rates, but overall characteristics were the same.

The experiments involving InP were performed using the doubled Ar<sup>+</sup> laser light (257 nm). The beam was focused onto the semiconductor surface to a spot size of 3  $\mu\text{m}$ . We have used relatively low power densities, i.e. from 50 to 3000 W/cm<sup>2</sup>, which is not high enough to cause thermally enhanced effects. The light enhanced etch rates of various dilute acidic solutions have been studied. A solution of dilute HF has shown fast etching rates up to 40  $\mu\text{m}/\text{min}$ . This solution exhibits a negligible dark etch rate and thus is suitable for maskless processing. To measure the light induced etch rates, shallow grooves were formed by scanning the semiconductor sample perpendicular to the laser beam. The features were measured afterwards using a stylus profilometer and/or a scanning electron microscope. The etched surface features shown in Fig. 15 were smooth, well-defined, and of suitable morphology for various electrooptical device applications. Figure 4 shows the etch rate as a function of the light intensity on the sample surface. The etch rates were determined by measuring the depth of the features divided by the

exposure or dwell time. As shown, it is linear in the low power regime and saturates due to transport limitation at a power density of  $100 \text{ W/cm}^2$ . This power dependency is very similar to the results measured for GaAs. The difference between InP and GaAs etching, is probably due to a slower dissolution process for InP which starts to limit the etch rates in the transport-limited region at a lower level.

FIGURE CAPTIONS

- Figure 1: Normalized resistivity for In lines as a function of the trimethylindium gas pressure.
- Figure 2: Low magnification scanning electron micrograph of a repaired MOSFET circuit.
- Figure 3: (a) Normalized resistivity of molybdenum lines as function of the incident laser power.  
(b) Thickness of the deposited molybdenum lines as function of the laser power.
- Figure 4: Diagram of the coordinate system used in solving the diffusion-limited photodeposition rate equation.
- Figure 5: Time to 1/e transmission point versus laser spot size for  $T=25^{\circ}\text{C}$  and  $T=70^{\circ}\text{C}$ . The 1/e transmission point is inversely proportional to the deposition rate.
- Figure 6: Growth rate of metal gratings versus grating spacing grown by photodeposition from diethylcadmium on a quartz window.
- Figure 7: SEM micrographs of a via hole etched through a  $250\mu\text{m}$ -thick GaAs sample:  
A) via-hole entrance, and B) cleaved cross section.
- Figure 8: (a) SEM micrograph of a hole and slits etched through a GaAs wafer.  
(b) Comparison of the etched profile with free-space propagation of the focused laser beam.
- Figure 9: (a) SEM micrograph of the temporal development of the vertical via hole.  
(b) Initial, Gaussian-shape etchings.  
(c) Formation of tubular, non-Gaussian profiles.
- Figure 10: Attenuation coefficient of this hollow GaAs waveguide as a function of hole diameter, measured for 257-nm and 514-nm wavelengths.
- Figure 11: Experimental arrangements for the projection etching.
- Figure 12: Projection etching of GaAs: 4:1 imaging.
- Figure 13: Calculated hole development with (solid line) and without (dashed line) first internal reflection.
- Figure 14: Etch rates for n-type silicon as a function of laser intensity.
- Figure 15: SEM micrographs of a slit etched in an InP wafer.
- Table 1. Excimer laser etching of different doping types of (100) GaAs. The incident pulse energy was  $\mu\text{J}/\text{cm}^2$ .

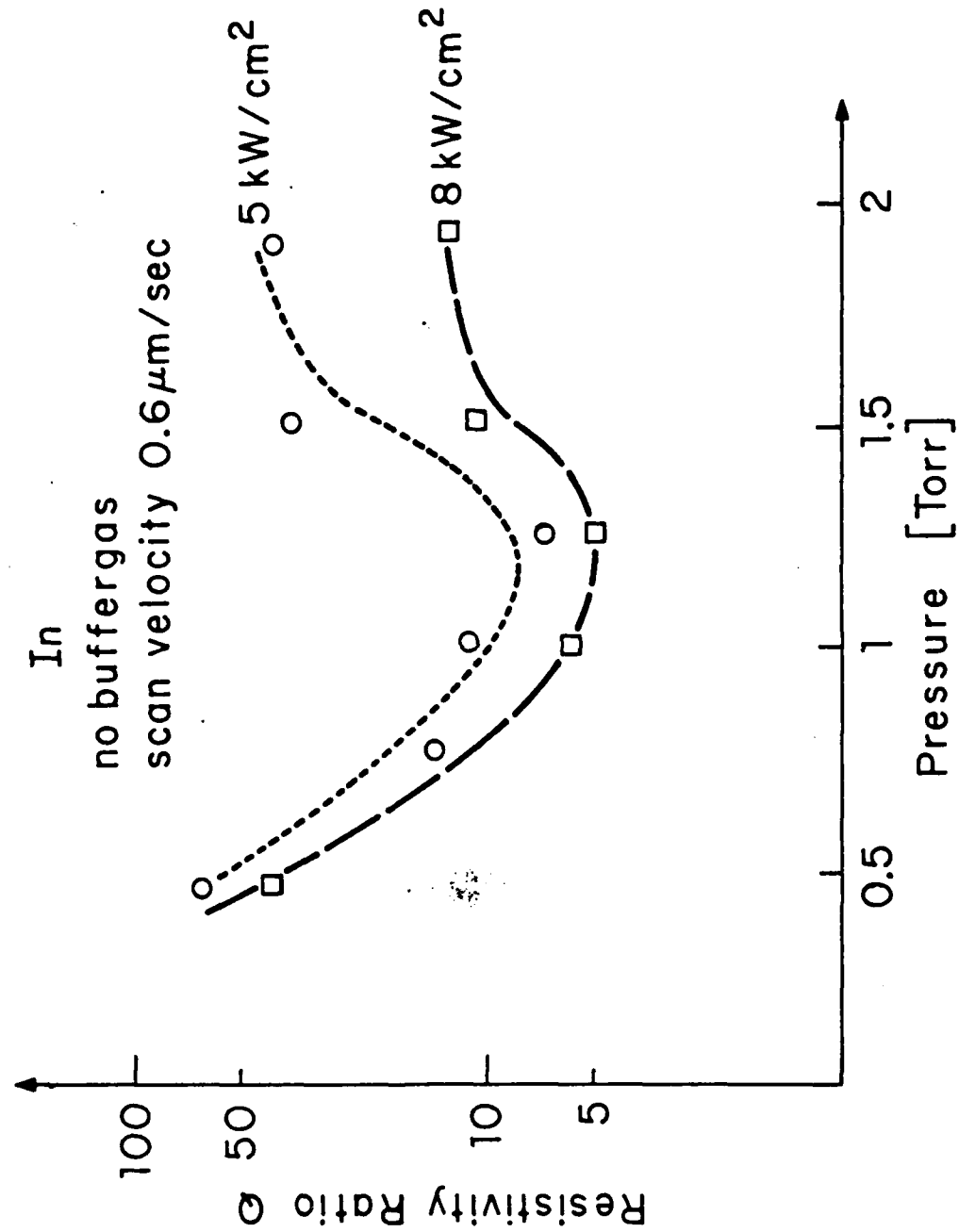


Figure 1.



# IC REPAIR

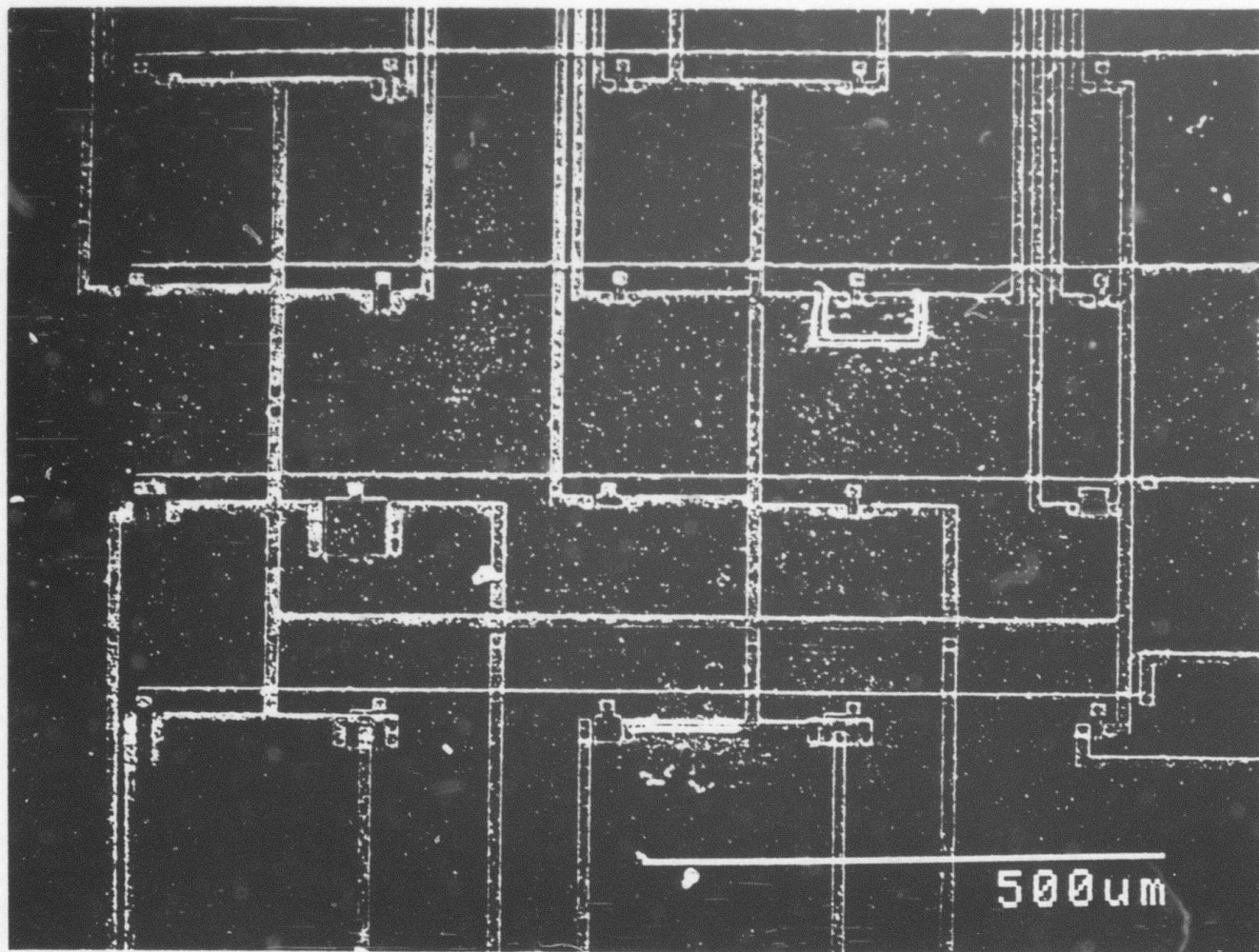


Figure 2.

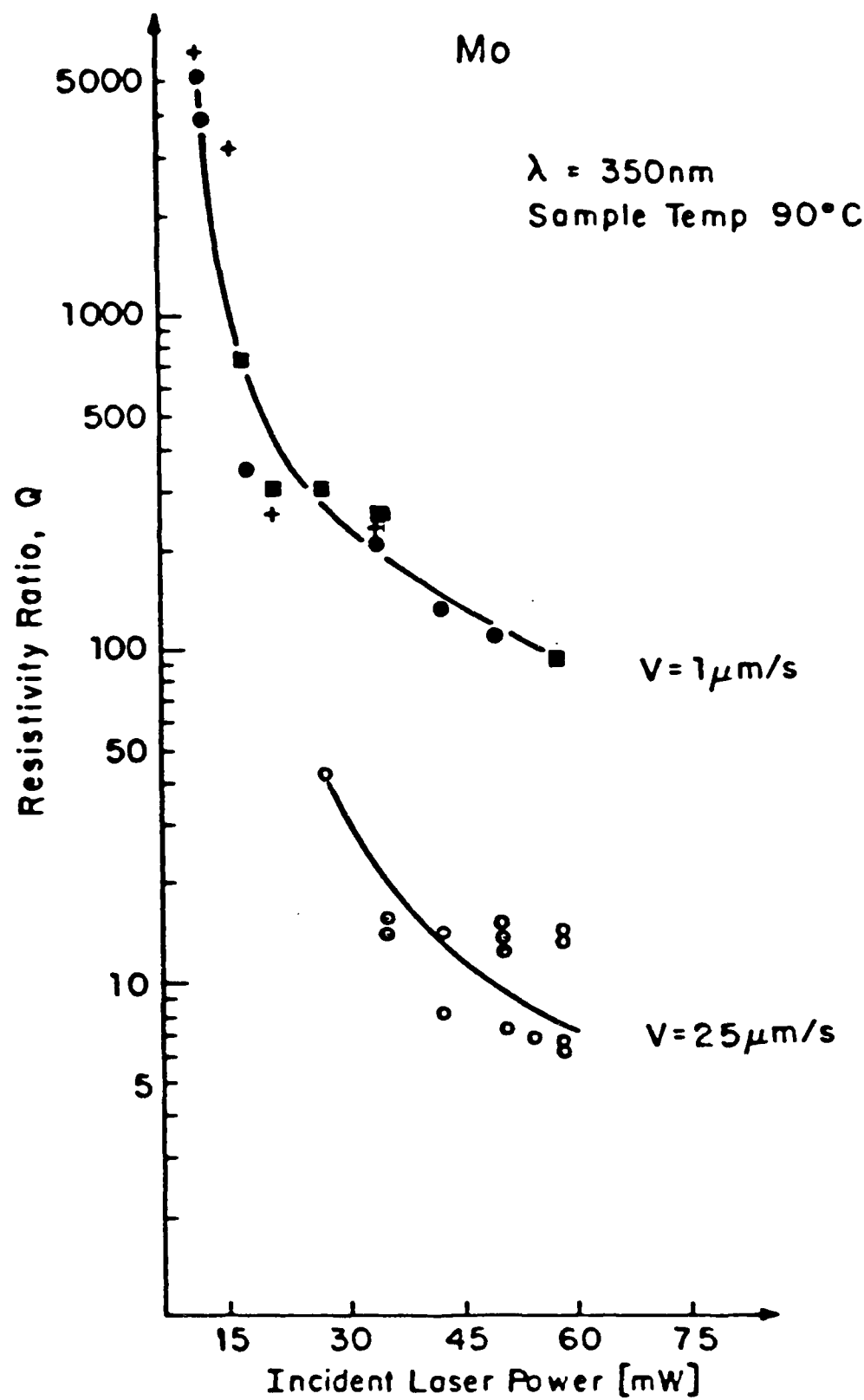


Figure 3a.

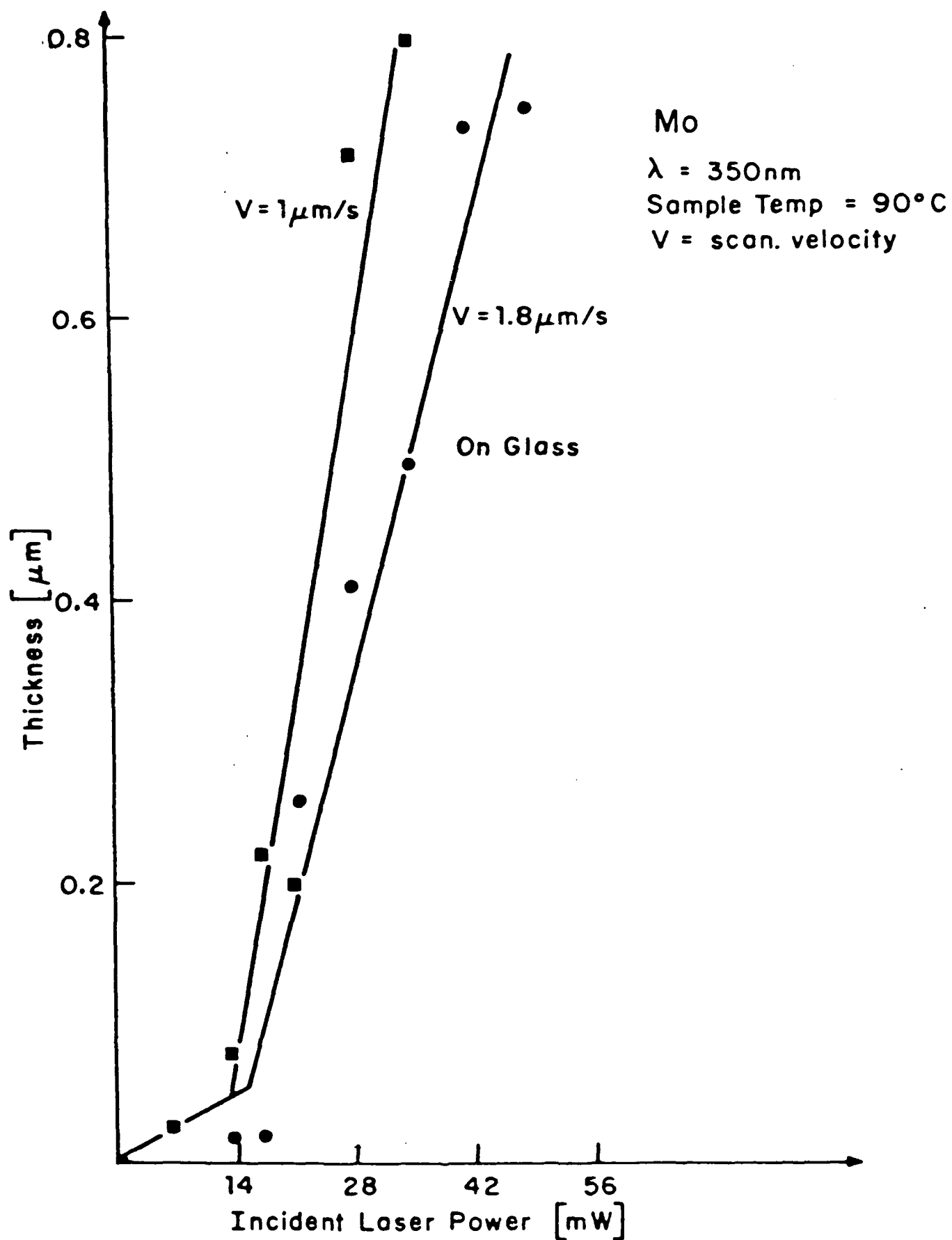


Figure 3b.

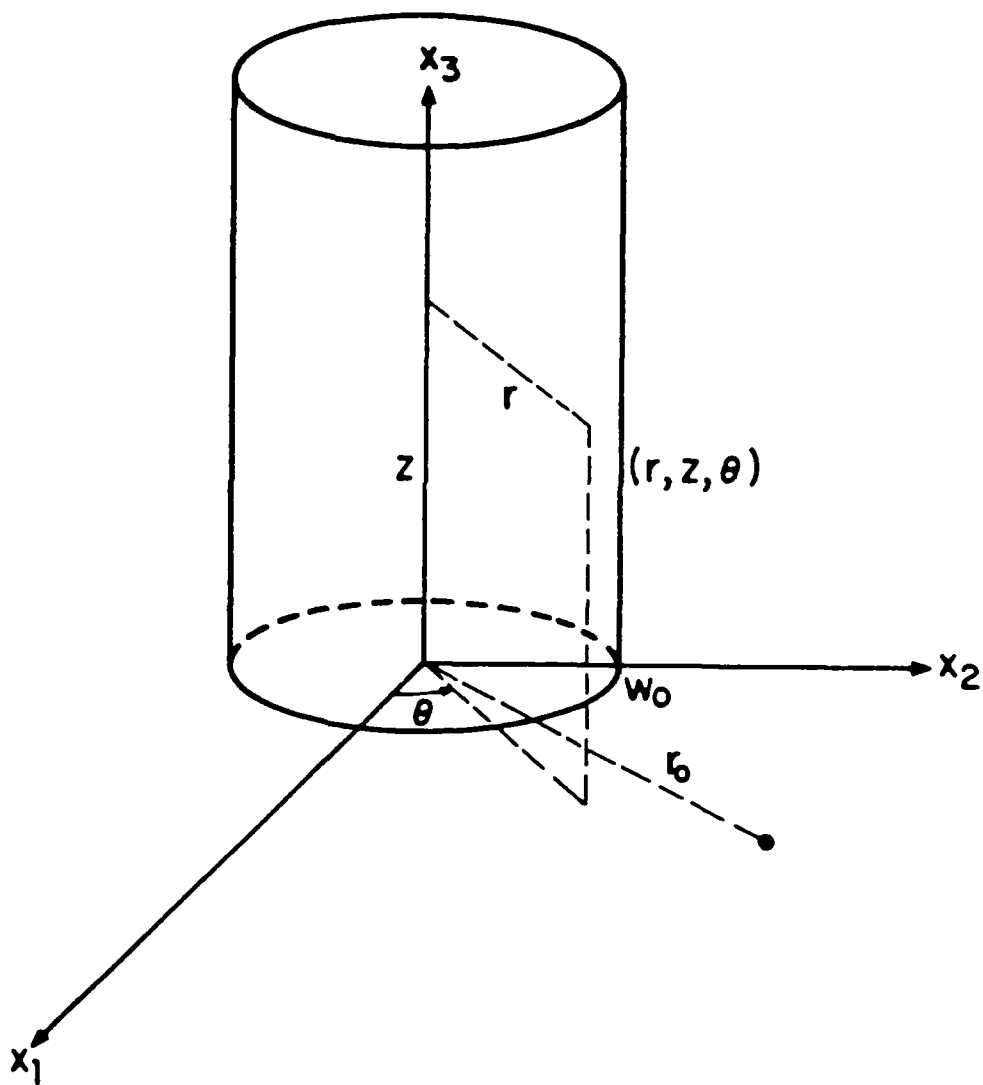


Figure 4.

A-66-3042 JD

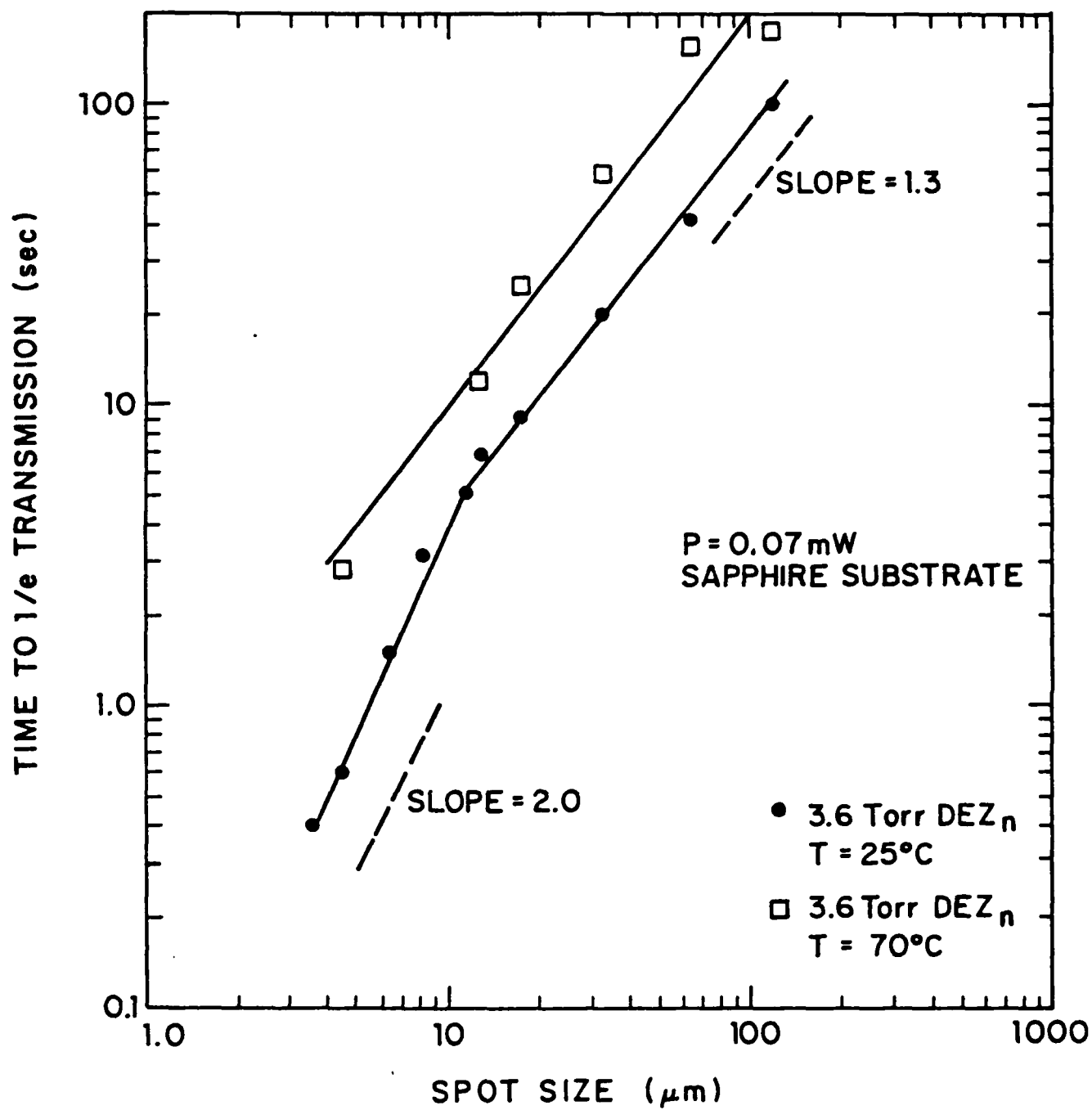


Figure 5.

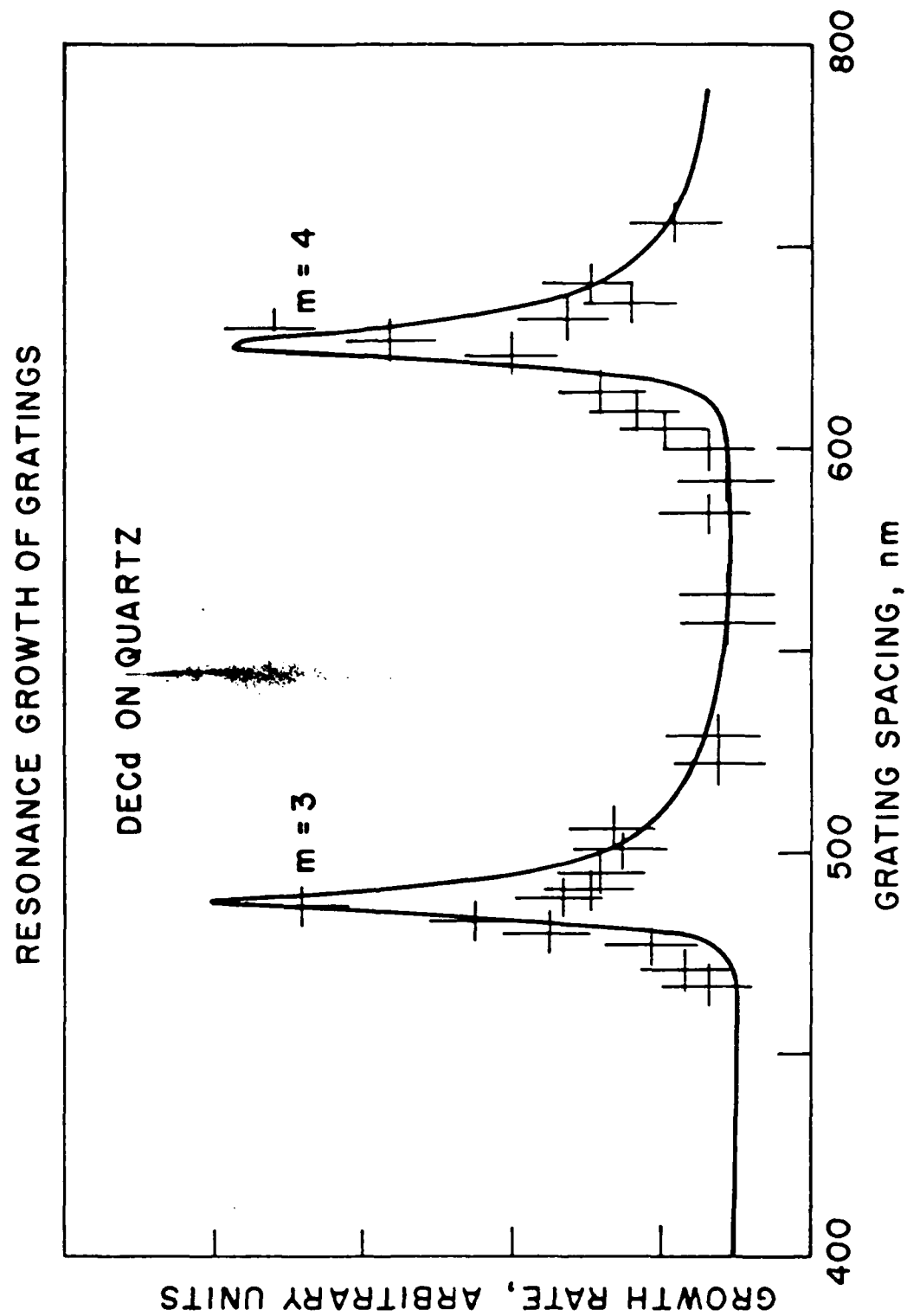
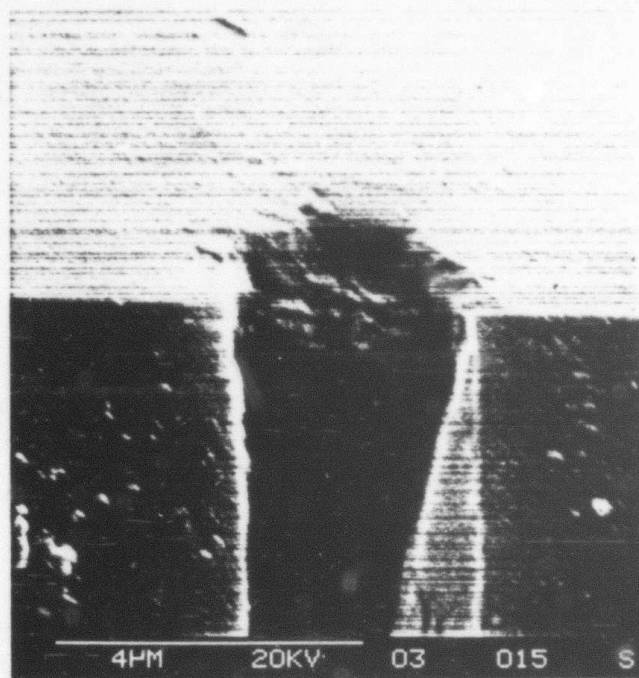


Figure 6.

a



b

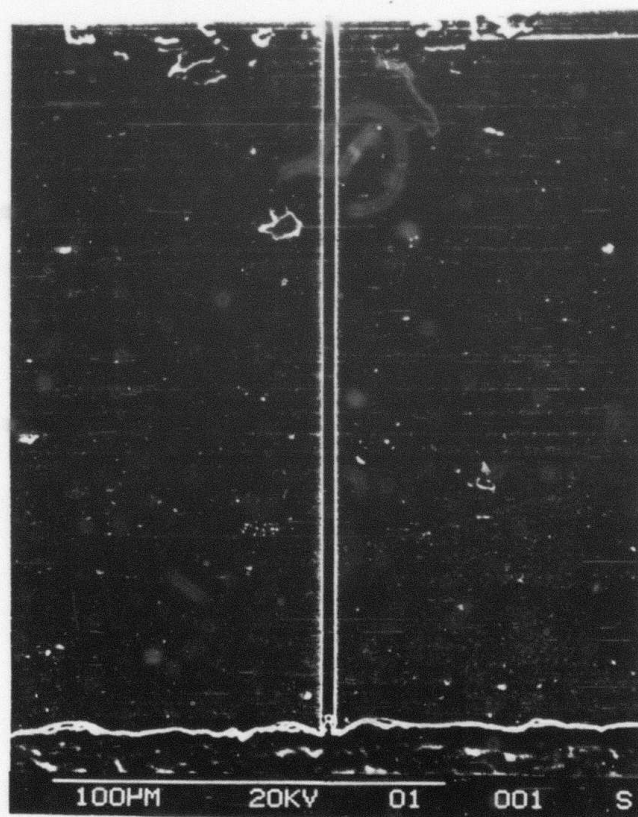
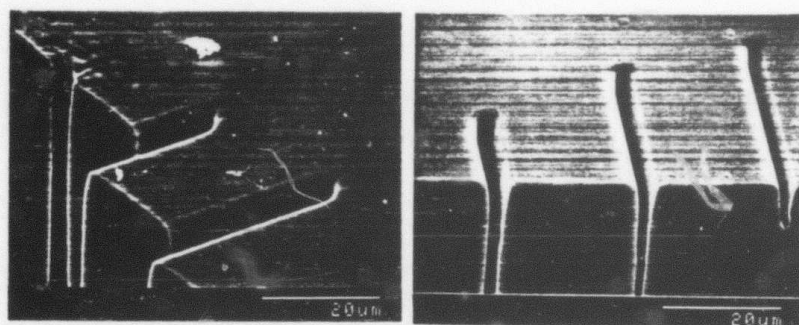
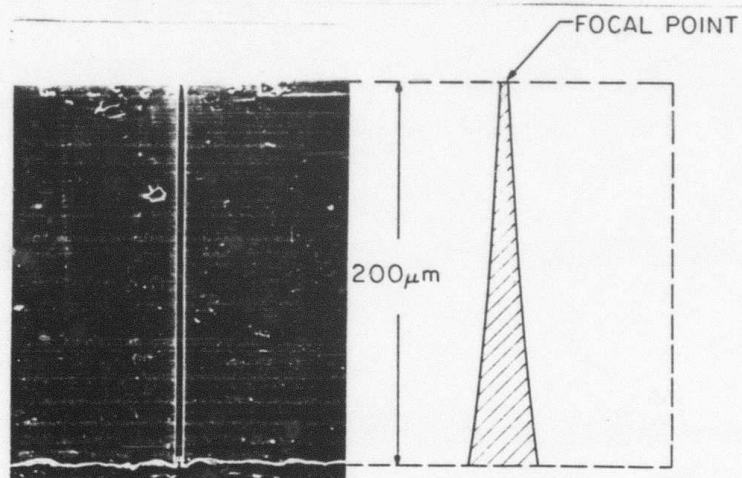


Figure 7.



a



b

Figure 8.



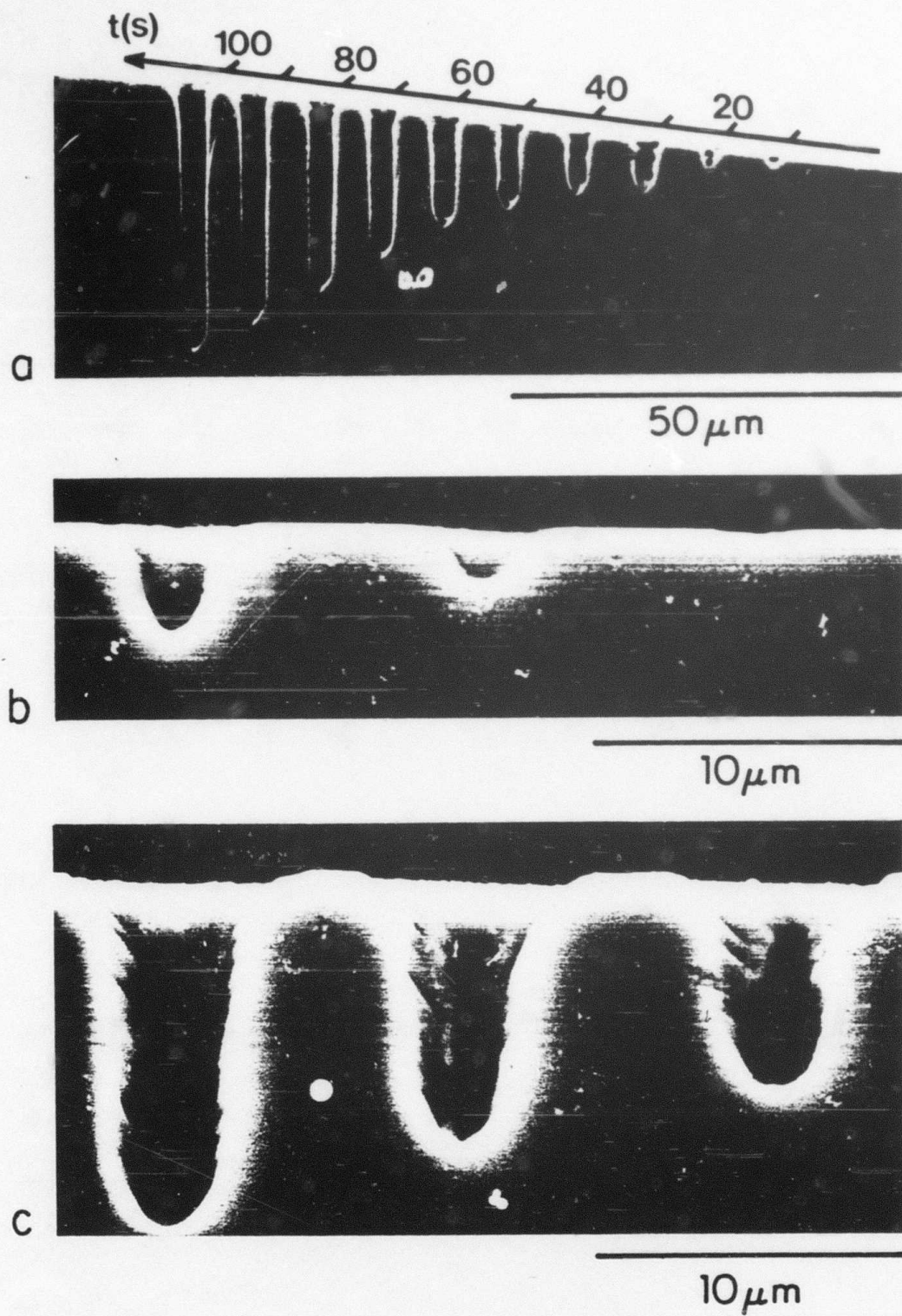


Figure 9.

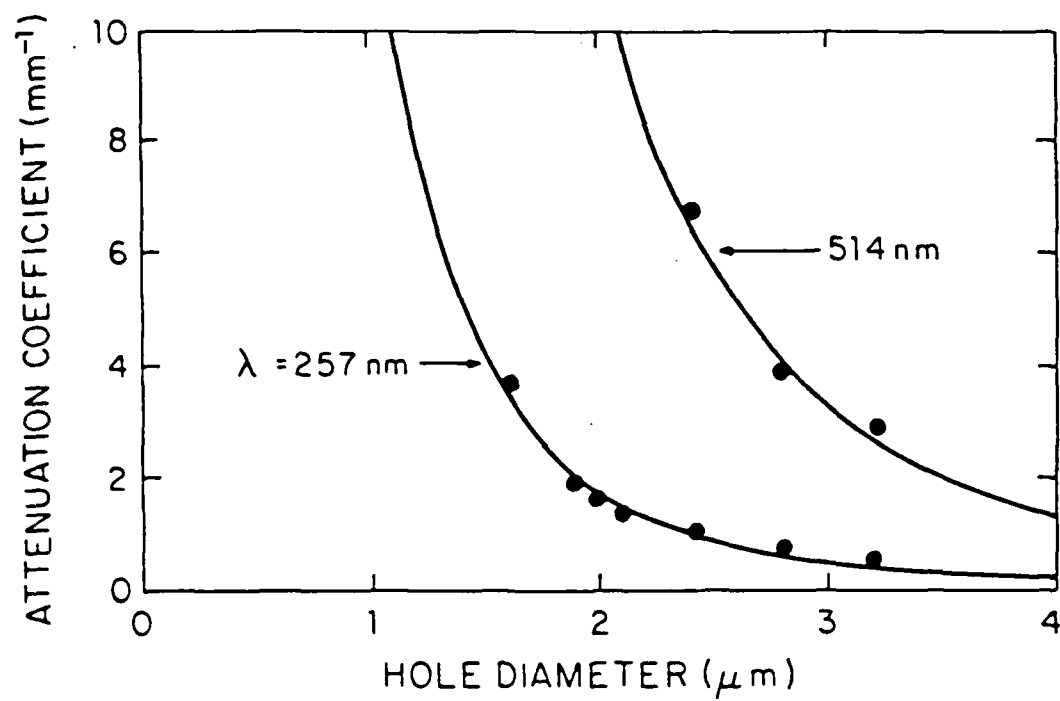
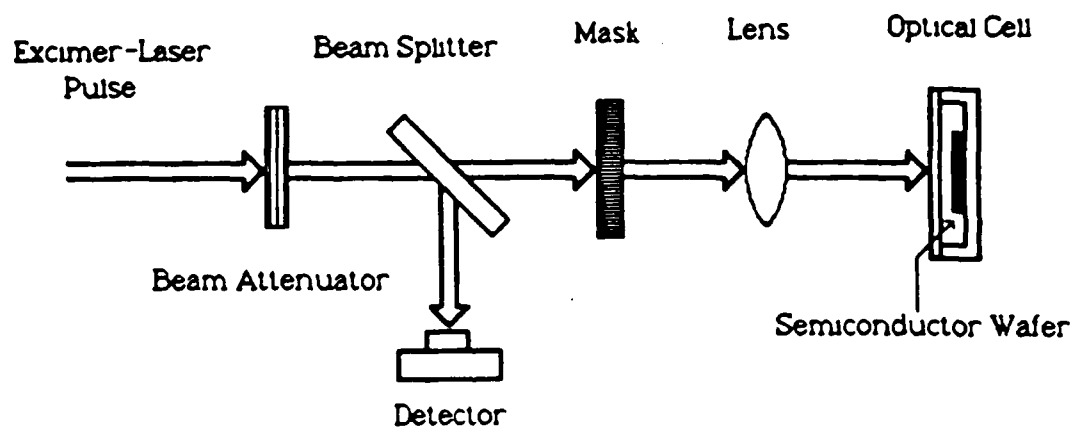


Figure 10.

## Excimer Laser Processing : Wet Etching of GaAs



Optical Imaging



Figure 11.

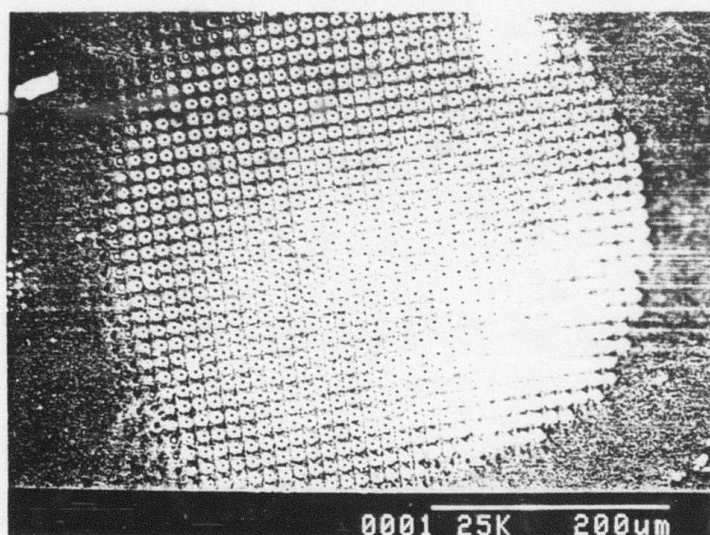
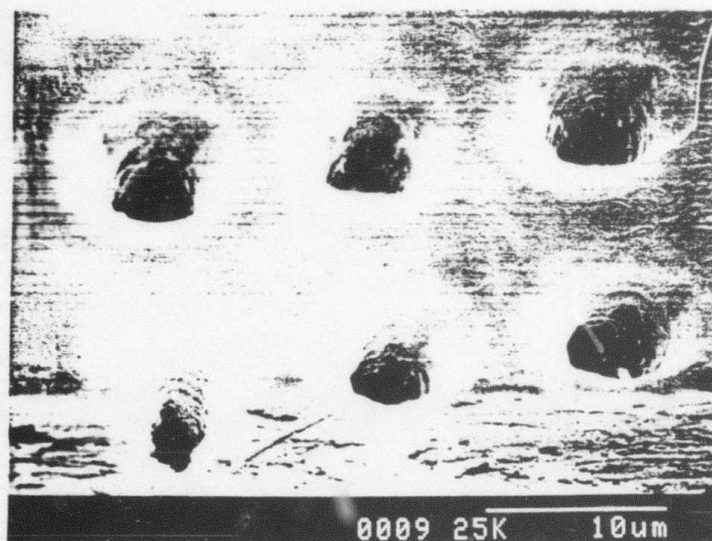


Figure 12.

EFFECT OF INTERNALLY  
REFLECTED LIGHT ON  
WAVEGUIDE FORMS

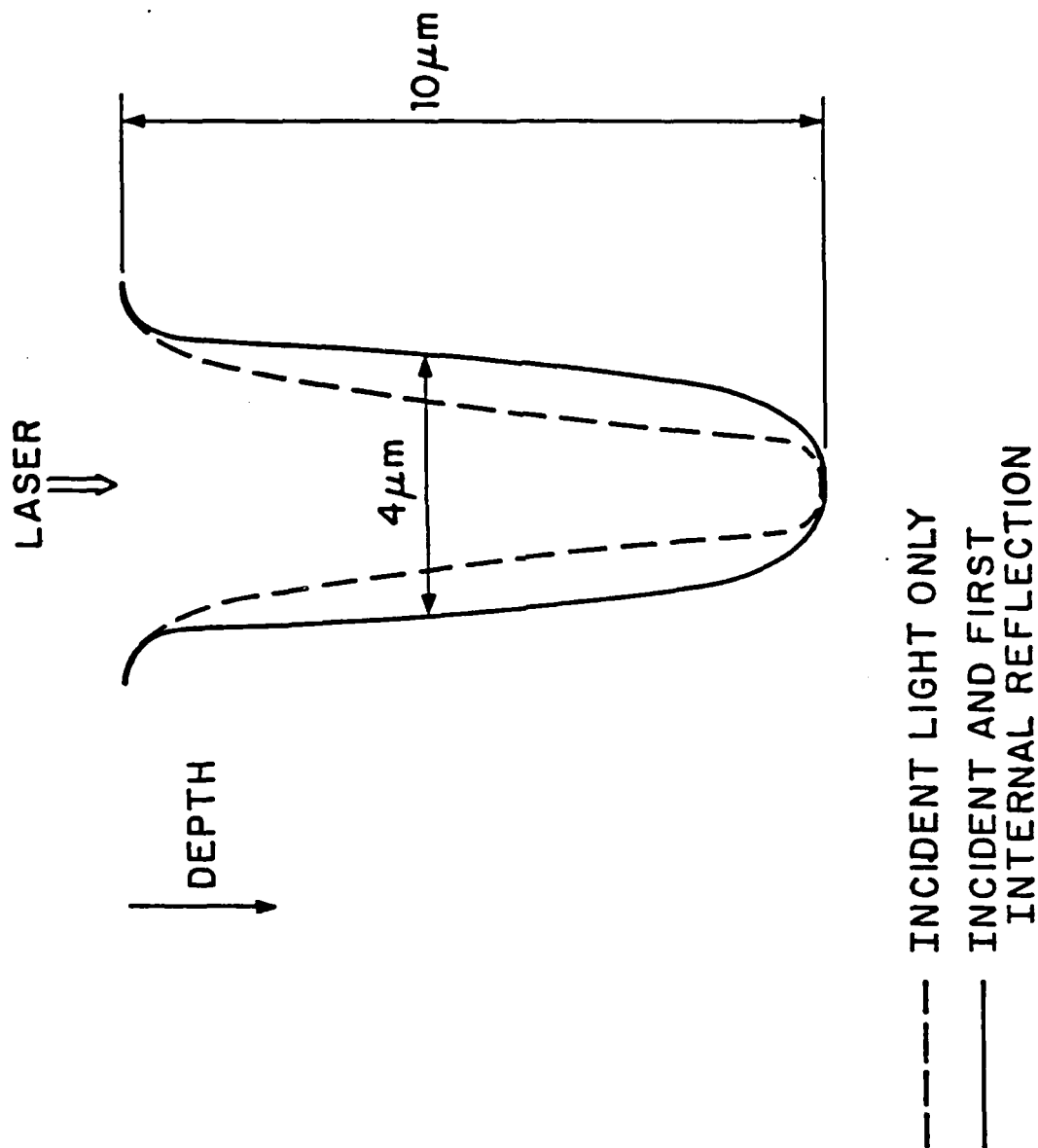


Figure 13.

## Si ETCHING RATE

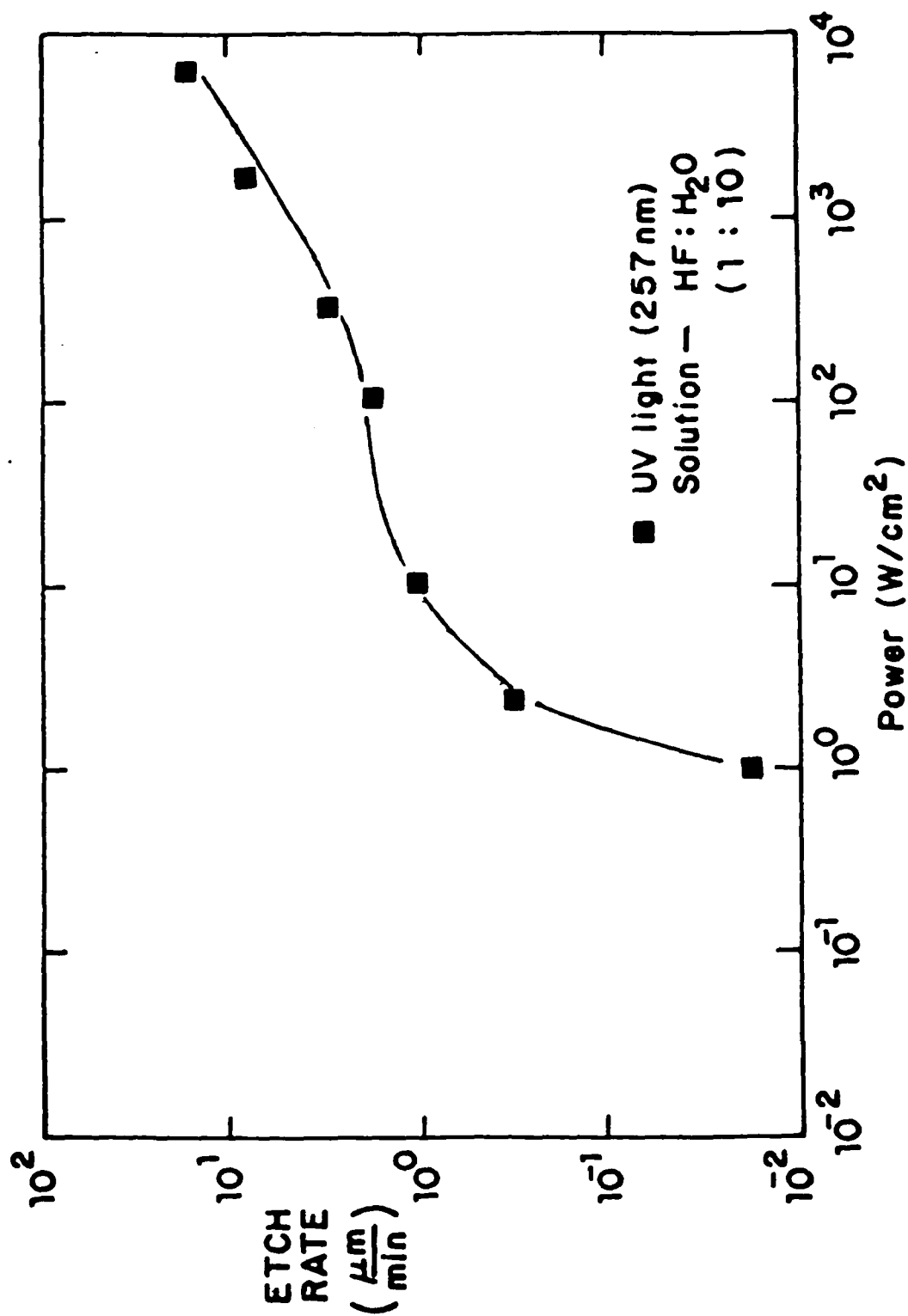


Figure 14.



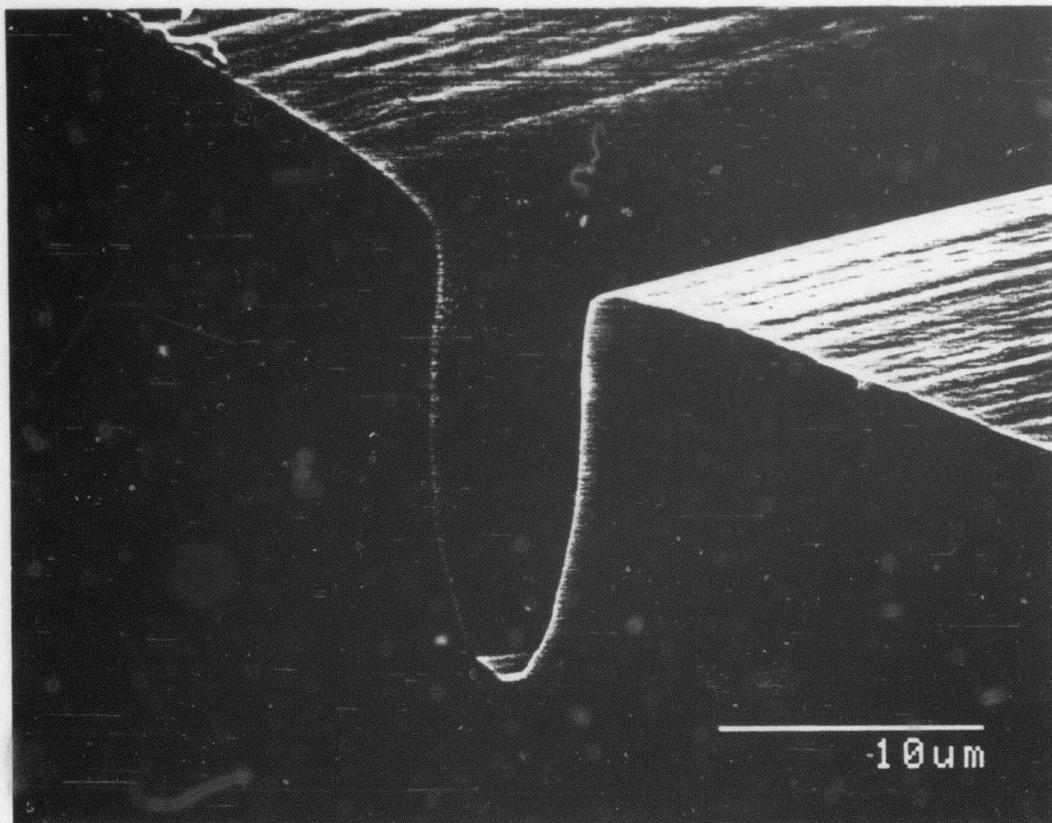


Figure 15.

	n-GaAs	SI-GaAs	p-GaAs
Etch Rate (nm/min)	240	170	30

Table 1.



PAPERS SUBMITTED FOR PUBLICATION BASED ON WORK IN THIS CONTRACT

1. D. Podlesnik, H.H. Gilgen, R.M. Osgood, "Deep-Ultraviolet Wet Etching of GaAs," Appl. Phys. Lett. 45, 563 (1984)
2. W. Holber, G. Reksten, R.M. Osgood, "Laser-Assisted Dry Etching of Materials," Proc. of SPIE 459, 129 (1984)
3. H. Gilgen, C.J. Chen, R.R. Krchnavek, R.M. Osgood, "The Physics of Ultraviolet Photodeposition," Laser Processing and Diagnostics ed., D. Bauerle (Springer Series on Chemical Physics, Berlin, 1984) 39, 225.
4. R.R. Krchnavek, H.H. Gilgen, R.M. Osgood, "Maskless Laser Writing of Silicon Dioxide," J. Vac. Sci. Tech. B, 641 (1984)
5. D. Podlesnik, H.H. Gilgen, R.M. Osgood, "Deep-Ultraviolet Induced Wet Etching of GaAs," Appl. Phys. Lett. 45, 563 (1984)
6. P. Brewer, G. Reksten, R.M. Osgood, "Laser-Assisted Dry Etching," Solid-State Science Technology, 273, April (1985)
7. W. Holber, G. Reksten, R.M. Osgood, "Laser Enhanced Plasma Etching of Silicon," Appl. Phys. Lett. 46, 201 (1985)
8. R.M. Osgood and T.F. Deutsch, "Laser-Induced Chemistry for Microelectronics," Science, 227, 709 (1985)
9. C.J. Chen, H.H. Gilgen, R.M. Osgood, "Resonant Optical Growth of Submicrometer Metal Gratings," Optics Lett. 10, 173 (1985)
10. R.M. Osgood and H.H. Gilgen, "Laser Direct Writing of Materials," Ann. Rev. of Mat. Sci. 15, 549 (1985)
11. D.V. Podlesnik, H.H. Gilgen, R.M. Osgood, "Waveguiding Effects in Laser-Induced Aqueous Etching of Semiconductors," Appl. Phys. Lett. 48, 496 (1986)

PAPERS SUBMITTED FOR PUBLICATION (Cont'd)

12. D.V. Podlesnik, H.H. Gilgen, R.M. Osgood, "Direct, Maskless Fabrication of Submicrometer Gratings on Semiconductors," Proc. SPIE Int. Soc. Opt. Eng. 560, 1985 (in press)
13. P.R. Prucnal, E.R. Fossum, R.M. Osgood, Jr., "Integrated Fiber-Optic Coupler For Very Large Scale Integration Interconnects," Optics Lett. 11, No.2, 109 (1986)

PRESENTATIONS TO INDUSTRY AND PROFESSIONAL ORGANIZATIONS

Workshop on Lightwave Technology	Los Angeles	Jan. '84
SPIE Symposium on Laser Chemical Processing	Los Angeles	Jan. '84
General Electric Research Labs	Schenectady	Feb. '84
ITT Research	Shelton	Feb. '84
APS Annual Meeting (Invited)	Detroit	Mar. '84
Rank Prize Minisymposium on Laser Writing	Malvern	April '84
Philips Research Laboratory	Briarcliff	April '84
Rank Prize Minisymposium on Laser Writing (Keynote Address)	Malvern	April '84
CLEO 85 2 talks	Los Angeles	June '84
International Quantum Electronics Conference	Los Angeles	June '84
Motorola (Special Presentation)	New York City	June '84
Conf. on Laser Processing and Diagnostics	Linz	July '84
Gordon Conf. on Plasma Processing in Microelectronics	New Hampshire	July '84
Conf. on Solid-State Devices and Materials	Kobe	Sept. '84

PRESENTATIONS TO INDUSTRY AND PROFESSIONAL ORGANIZATIONS (Cont'd)

ACS Meeting	Philadelphia	Sept. '84
Materials Research Society Symposium on Laser Chemical Processing - (1 Invited, 4 Contributed)	Boston	Nov. '84
University of Bern	Bern	Jan. '85
SRC Presentation	New York City	Jan. '85
Perkin-Elmer	Danbury	Feb. '85
Symposium on Laser and Ion Beam Surface Microphysics	Santa Fe	Feb. '85
Gordon Conference	Santa Barbara	Feb. '85
Philips (Special Symposium)	New York City	Mar. '85
University of Toronto, Laser Colloquium	Toronto	Mar. '85
IBM Plasma Symposium (Invited)	Burlington	May '85
GE Whitney Symposium (Invited)	Schnectady	June '85
SRC <u>In Situ</u> Processing Symposium (Invited)	Research Triangle	June '85
NSF Symposium on Processing Electronics Materials	Newark, Delaware	June '85
SPIE Conference on Diffraction Phenomena in Optical Engineering Applications	San Diego	Aug. '85
IBM Special School on Lasers and Applications	Lech	Aug. '85
Electrochemical Society Fall Meeting (Invited)	Las Vegas	Oct. '85
American Vacuum Society	Houston	Nov. '85
Materials Research Society Symposium on Beam Processing -(1 Invited, 4 Contributed)	Boston	Nov. '85